Orientation of elongated particles in shear and extensional flow

by

Karl Håkansson

May 2012
Technical Reports from
Royal Institute of Technology
KTH Mechanics
SE-100 44 Stockholm, Sweden

Akademisk avhandling som med tillstånd av Kungliga Tekniska Högskolan i Stockholm framlägges till offentlig granskning för avläggande av teknologie licentiatexamen den 15 Juni 2012 kl 14.00 i seminarierummet, Brinellvägen 32, Kungliga Tekniska Högskolan, Stockholm.

Universitetsservice US–AB, Stockholm 2012

Karl Håkansson 2012, **Orientation of elongated particles in shear and extensional flow**

Wallenberg Wood Science Center & Linné FLOW Centre, KTH Mechanics
Royal Institute of Technology
SE–100 44 Stockholm, Sweden

Abstract

Elongated particles in fluid flows are a big part of the world we are living in. Gaining knowledge on how particles behave in different fluid flows can potentially increase the efficiency of industrial processes and decrease the world's energy consumption as well as improve the properties of future materials.

In this thesis, the orientation of elongated particles in two different flows are studied. The first case is a dilute fibre suspension in a turbulent flow and the second case is a semi-dilute fibril dispersion in a laminar flow. The fibres (cellulose acetate) are at least three orders of magnitude larger than the fibrils (nano-fibrillated cellulose).

The turbulent flow case is half of a full channel flow, characterised by the friction Reynolds number, and is experimentally examined. This experiment is closely related to the papermaking process. Laser Doppler velocimetry measurements are preformed without fibres in order to make sure that the flow is turbulent and fully developed. Images of the fibres in the flow are acquired using a CCD-camera, from which it is possible to detect the fibres in an image processing step and extract both the positions and orientations of the fibres. A large parameter study is carried out, where the aspect ratio of the fibres, concentration and Reynolds number are changed. Short fibres are observed to align perpendicular to the flow, while the longer fibres are found to align in the flow direction. The fibres are also seen to accumulate in streamwise streaks, believed to be caused by velocity structures in the turbulent flow.

The second flow case studied focusses on a semi-dilute dispersion in a laminar flow. It includes both experiments and numerical calculations of the fibril orientation. The aim of this study is to demonstrate that it is possible to control the fibril orientation with a fluid. In a semi-dilute dispersion, fibrils are interacting. However, no flocs or networks are formed. A flow focusing apparatus is used in order to hydrodynamically accelerate the dispersion with an outer fluid (sheath) flow. The mean orientation in the flow direction is experimentally studied by detecting the birefringence of the flowing dispersion. The orientation distribution is calculated by solving the Smoluchowski equation. The fibrils are seen to align in the flow direction both in the experiments and the calculations. Moreover, the alignment is found to increase with increasing acceleration.

Descriptors: Orientation, fibre, fibril, turbulent channel flow, particle streaks, flow focusing, nano-fibrillated cellulose, extensional flow, Smoluchowski

Preface

This licentiate thesis in fluid mechanics considers the orientation of elongated particles in two different flows; one turbulent and dilute, and the second laminar and semi-dilute. The work is experimental with the addition of a numerical comparison for the second case. The thesis is divided into two parts; Part I provides an overview and summary of the work, with chapters presenting relevant applications, summaries of the two experiments, a discussion and outlook, followed by a chapter describing the author's contributions to the three papers. Part II consists of three papers describing the work in detail.

May 2012, Stockholm
Karl Håkansson

Part of this work has been presented by the author at:

2nd SIG43 workshop on fibre suspension flows,
9 – 10 February 2010, *Stockholm, Sweden*

Ekmandagarna,
25 – 26 January 2011, *Stockholm, Sweden*

3rd SIG43 workshop on fibre suspension flows,
6 – 8 April 2011, *Udine, Italy*

Svenska mekanikdagarna,
13 – 15 June 2011, *Göteborg, Sweden*

8th International Conference on Flow Dynamics[1],
9 – 11 November 2011, *Sendai, Japan*

Part of this work have been presented by coauthors at:

7th International Conference of Multiphase Flows [2],
30 May – 4 June 2010, *Tampa, Florida, USA*

SPCI event,
17 – 19 May 2011, *Stockholm, Sweden*

SIAMUF seminarium,
20 – 21 October 2011, *Göteborg, Sweden*

[1]The presentation received a *"Best poster"* award
[2]With written contribution to the conference proceedings: M. Kvick, K. Håkansson, F. Lundell, L. Prahl Wittberg and L. D. Söderberg: Fibre Streaks in Wall Bounded Turbulent Flow.

Contents

Part I

Overview & summary

CHAPTER 1

Introduction

When two or more materials of different phases, *e.g.* one solid and one liquid, or two (or more) immiscible materials of the same phase are flowing the flow is said to be a multiphase flow. Such flows are present in a wide range of systems in the world, both in nature and industry. This thesis focuses on the behaviour of solid fibres/fibrils in flowing water suspensions/dispersions. The fibrils are here three orders of magnitude smaller than fibres. A dispersion is a system where the solids are small enough to have a different density than the liquid but still be in a stable state, whereas the suspension is a mixture of a liquid and solids, where the solids are too large to be in a stable state.

In this chapter, the modern papermaking process, where multiphase flows are present and important, will be described. For references considering this section, see Norman *et al.* (2005); Lundell *et al.* (2011). Thereafter, there will be a short introduction to composites. The third section is introducing a bio material with expectations to have a big impact in future composite materials. The scope of the present work will be described in the final section.

1.1. Papermaking

Making paper from wood is a very old tradition, going all the way back to 2^{nd} century China. In those days, each sheet was made by hand. Nowadays huge paper machines produce vast amounts of paper in a continuous process.

The raw material used to make paper is wood pulp, consisting of wood fibres with diameters of about 20 μm and lengths of $0.5 - 3$ mm. The wood pulp can be produced either mechanically or chemically by breaking wood chips apart. It is also possible to use a combination of both.

In a modern paper machine, the pulp, composed of $\sim$ 1% wood fibres and $\sim$ 99% water, is pumped into a headbox, that jets the pulp out onto a dewatering wire. The water is pressed out in a pressing stage and a fibre network is formed. Thereafter a heating (drying) step is needed in order to get the paper completely dry.

A headbox is depicted in figure 1.1, where the thickness of the headbox jet is of the order of 1 cm, the width is up to 10 m and the velocity as high as 30 m/s. The purpose of the headbox is to distribute the fibres as homogeneously as possible. The flow inside the headbox is both accelerated, to break up

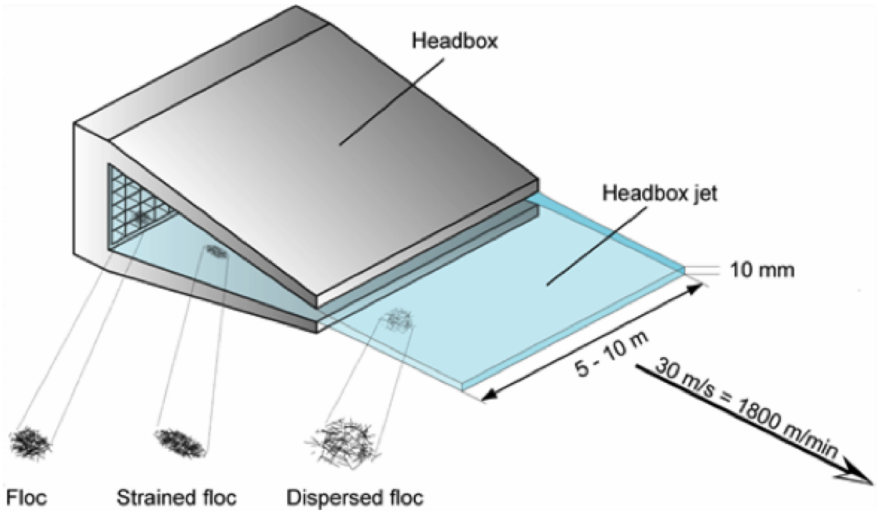

FIGURE 1.1. The headbox of a paper machine, courtesy of L.D. Söderberg.

flocs, and turbulent to mix the pulp. The reason for this is that breaking up fibre flocs, mixing of fibres and controlling the orientation of the fibres are key parameters to a good final paper.

The strength of the paper is to a large extent determined by the fibre orientation distribution, and especially in which direction the paper is strong, see Cox (1952). The flow in the headbox influences the fibres and their orientation in different ways, acceleration in one way and the turbulence and shear in others.

One measure of paper smoothness is the formation. Examples of good and bad formation are shown in figure 1.2, where the formation is quantified by the intensity variations within each image. A piece of paper with well distributed and defloculated fibres has good formation and vice versa. The turbulence is responsible for both breaking up and forming flocs in the headbox, where the fibre size and the turbulent scales are important parameters in order to get good formation. The formation is a very important property since it determines the minimum amount of fibres needed to produce a paper with certain minimum thickness. If the formation is good, the thickness variation is low.

1.2. Composites

A composite is the product of combining two or more different and separable materials. The properties of a composite are enhanced as compared to the properties of the constituents themselves. In order to control the composite's

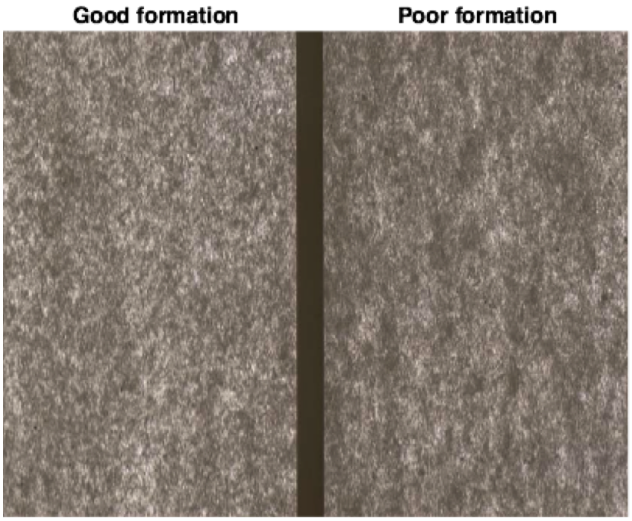

FIGURE 1.2. Examples of good and bad formation of a piece of paper, courtesy of L.D. Söderberg.

properties, it is desirable to control the structure of the constituents. A composite usually consists of a matrix material and a load bearing material, where the load bearing material most commonly consist of elongated solid particles such as a fibres. The structure properties can, for example, be the orientation of the fibres, the volume fraction or interaction between fibres.

1.3. Nano-Fibrillated Cellulose, NFC

Cellulose is one of the most abundant polymers in the world, and is found in wood, plants and bacteria, in different sizes and quantities. Here the focus is on wood. Wood is built up by fibres typically composed of one third of cellulose, one third of lignin and one third of hemicelluloses, see *e.g.* Norman *et al.* (2005) and references therein. The strength of the wood fibres is correlated to the long straight cellulose chains, where the lignin act as the matrix and the hemicelluloses interconnects the cellulose with itself and lignin. Cellulose polymer chains do not appear one by one in the cell wall, but rather as bundles of polymer chains, called fibrils. The fibre cell wall is built up by different layers in which the cellulose fibrils have different preferred orientation, with respect to the fibre direction. The outermost layer has a random fibril-orientation distribution, the second close to 90°, the third a smaller angle $10° - 30°$ and the last layer close to 90° again. These different orientations makes it possible for the tree to withstand both compression and bending. Tuning the orientation

of the fibrils in man-made materials could potentially give rise to a wide range of different properties.

If the cellulose fibrils withhold their size and structure while extracted and separated from the wood, the outcome is called Nano-Fibrillated Cellulose, NFC, see Eichhorn *et al.* (2010). The typical length of a fibril is $1 - 3$ μm and the diameter is $20 - 40$ nm. One single crystalline cellulose polymer has experimentally been found to have an elastic modulus of 140 GPa, see Sakurada *et al.* (1962) compared to $\sim$ 20 GPa for plant fibres, see Morton & Hearle (1975). The fibrils are expected to have properties very close to the crystalline cellulose polymer, since a fibril consists of approximate $15 - 20$ polymers.

The energy consumption of the extraction process has recently been greatly improved due to an enzymatic pre-treatment of the pulp, see Pääkkö *et al.* (2007). This allows for a more expensive post treatment of the NFC, without the sacrifice of a more expensive end product.

1.4. Scope of present work

There are many ways to study the interactions between fluid flows and elongated particles, both of macroscopic- and nano-scale size. Observing the orientation distributions in well defined flows provides insight to the dynamics of the systems and the interactions between particles and the fluid, as well as the interactions between two or more particles with each other.

The scope of this work is to experimentally observe and analyse the orientation distributions of elongated particles in two different flows, one laminar and one turbulent. In order to enable this, experimental techniques and data analysis methods are developed. A dilute suspension was used in the turbulent experiment, and a a semi-dilute dispersion in the laminar. Moreover, the fibre distributions were investigated numerically for the semi-dilute and laminar case.

The first experimental setup can be related to the headbox of a papermachine, where fibre-wall interactions frequently occur. The second setup was used to study the behavior of the NFC fibrils in a well defined flow, in order to control the fibril orientation in a future composite.

The aim of the laminar and semi-dilute experiment is not to study the process in details, but rather to test if it is possible to aligning fibrils with a fluid flow in an efficient manner.

A full literature review on every aspect touched upon in this thesis would result in a twice as thick thesis and is therefore not included. The goal is to combine information from many different areas and not to focus on one specific detail.

The first experiment was a close collaboration with Mr. Kvick, and the authors' contributions are described in chapter 5.

Chapter 2 describes and summarises the turbulent and dilute experiment, while chapter 3 is dedicated to the laminar and semi-dilute study. The discussion and future directions are found in chapter 4.

CHAPTER 2

Fibre orientation and fibre structures in wall bounded turbulent shear flow

In the headbox of a paper machine, the pulp flow is both accelerated and turbulent. Fibre flocs are formed and broken up and the orientation of the wood fibres in the dried paper is partly determined here. The fibre orientation is a key parameter in any composite, and correlated to the strength of the final product, see Cox (1952).

In the paper by Kvick *et al.* (2012), experiments with a dilute fibre suspension in a wall bounded turbulent shear flow were conducted. The low concentration made it possible to study the fluid flow interaction with particles without particle-particle interactions. A full description of the setup and the parameters are found in Kvick *et al.* (2012). The main purpose was to analyse the position- and orientation distributions of the fibres in the flow. And in order to do so, the fibres were dyed black and a camera was used to capture images of the fibres in the flow. An example image in the flow-vorticity plane (x-z) is displayed in figure 2.1. A large parameter study was carried out and the fibre orientation distribution and fibre position distribution was found for each experiment with the use of a steerable filter, evaluated in Carlsson *et al.* (2011). Selected results will be presented and discussed in this chapter.

2.1. Turbulent channel flow

A channel flow is defined as the flow between two plates, *i.e.* a rectangular geometry with high aspect ratio. Turbulent channel flow can be characterized by the friction Reynolds number, Re_τ;

$$\mathrm{Re}_\tau = \frac{hu_\tau}{\nu}, \tag{2.1}$$

where h is the half height of the channel, ν is the kinematic viscosity, $u_\tau = \sqrt{\tau_w/\rho}$ is the friction velocity and, τ_w and ρ are the wall shear stress and fluid density, respectively.

The experimental setup used in Håkansson *et al.* (2012*a*) and Kvick *et al.* (2012) consists of an open channel with water flowing down on a glass plate. The density and viscosity differences between the water and air makes it possible to approximate this experimental setup with half of a full channel. The

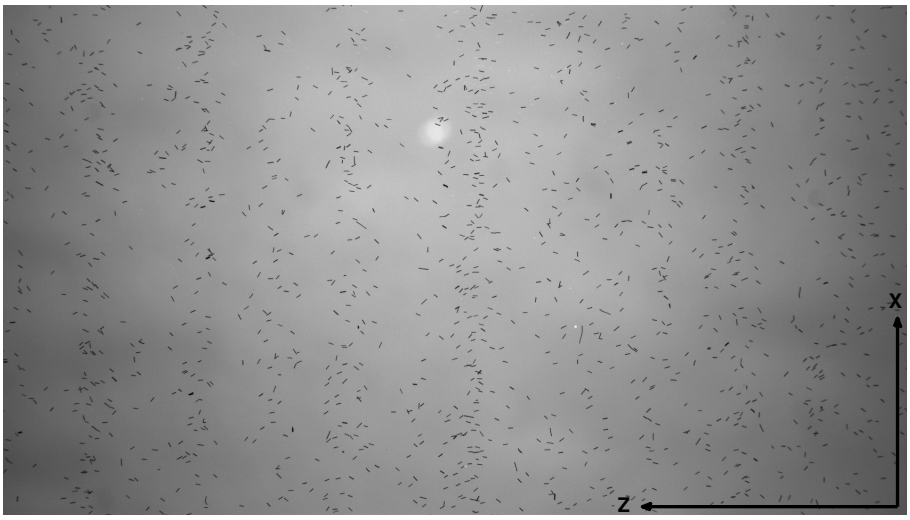

FIGURE 2.1. Image of black fibres in a turbulent shear flow, where the flow direction is upwards. The pysical size of the image is $\sim 5 \times 10$ cm.

surface velocity of the half channel is hence the same as the centreline velocity of the full channel. The flow velocities and fluctuations were experimentally measured by laser Doppler velocimetry, and the flow was concluded to be turbulent and fully developed at the image capturing location.

In channel flow as well as in boundary layers, high and low velocity streaks are present in the near wall region due to counter-rotating vortices, see Kim *et al.* (1987); Jeong *et al.* (1997); Matsubara & Alfredsson (2001); Lagraa *et al.* (2004). The velocity structures have been analysed by *e.g.* Zacksenhouse *et al.* (2001), reporting that the low speed streaks have a mean width of $\sim 50l^+$, where $l^+ = \nu/u_\tau$ is the viscous length scale.

2.2. Fibre orientation

In the experiment, the length of the sedimenting rigid cellulose acetate fibres ($\rho = 1300$ kg/m^3) was varied. Three different fibre lengths, $l = 0.5, 1$ and 2 mm having the same diameter, $d = 70$ μm, corresponding to aspect ratios, $r_p = l/d = 7, 14$ and 28 respectively, were used separately. The different aspect ratios are found to affect the orientation distribution heavily, as is displayed in figure 2.2. The short fibres, $r_p = 7$, are oriented perpendicular to the flow, 90°, while the long fibres, $r_p = 28$, are oriented in the flow direction, 0°, and the fibres with aspect ratio, $r_p = 14$, are oriented more isotropically. These three experiments were preformed at about the same friction Reynolds number based on a half channel height, $\mathrm{Re}_\tau \approx 125$. However, the same behaviour was

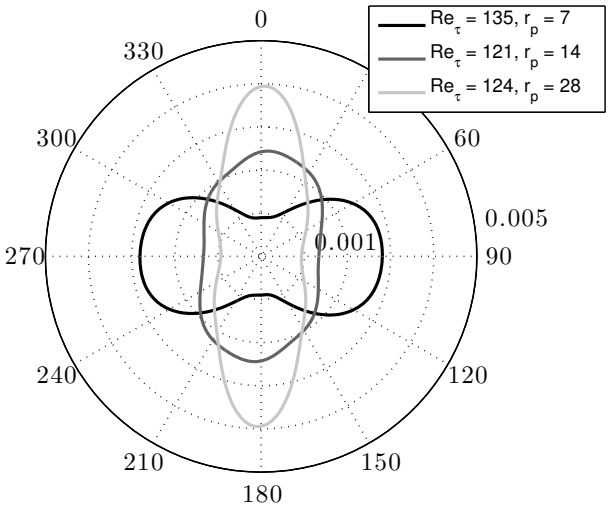

FIGURE 2.2. Orientation distributions for three cases corresponding to aspect ratios, $r_p = 7, 14$ and 28, where 0° is in the flow direction.

seen for most Reynolds number investigated, $\mathrm{Re}_\tau = 50 - 210$. The orientation distributions for fibres with $r_p = 7$ and 14 became more isotropic for $\mathrm{Re}_\tau > 200$.

In the studies by Carlsson *et al.* (2007) and Carlsson (2009) on fibre orientation in laminar flow a similar behaviour as in the present study was observed. It was concluded that the competing effects were the sedimentation and the wall contact versus fluid inertia. The sedimentation and direct wall contacts drives the fibre orientation towards the spanwise direction and the fluid inertia drives the orientation towards the flow direction.

As seen in figure 2.1, most of the fibres have a rather small out of plane angle, if any at all. This is in agreement with particles performing Jeffery orbits in laminar shear flow, Jeffery (1922). When particles perform Jeffery orbits, they remain in the x-z-plane most of the time, and periodically flip out of this plane. The rotation out of the x-z-plane may also be hindered by the fact that most fibres have sedimented and are very close to the glass plate.

2.3. Fibre structures

The fibres form fibre streaks for certain Reynolds numbers. These streaks are observed in figure 2.1. In order to understand how the fibres are affected by the fluid, quantitive measures are needed.

A quantification method for particle streaks was developed within the scope of this thesis. The method is described and evaluated in Håkansson *et al.* (2012*a*), where the two quantities provided are a streakiness measure, Ξ, and

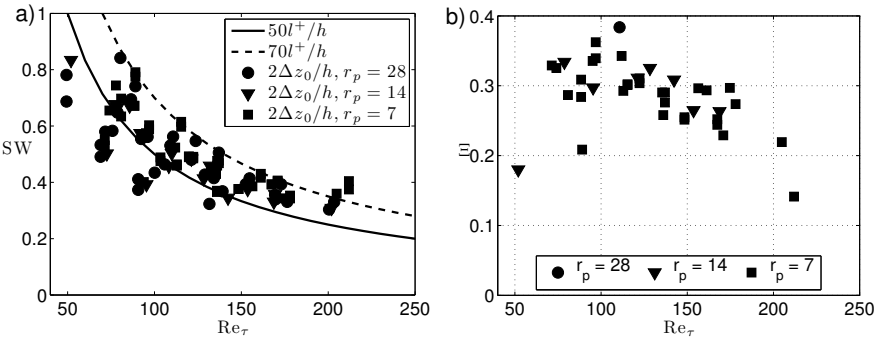

FIGURE 2.3. The streak width, SW, is shown in (a) and the streakiness, Ξ, in (b), versus Re_τ. The full and the dashed line in (a) corresponds to $50l^+$ and $70l^+$, respectively. The symbols, ($\blacksquare, \blacktriangledown, \bullet$), are experimental measurements where corresponding to $r_p = 7, 14, 28$, respectively, in both (a) and (b)

a mean streak width, $SW = 2\Delta z_0$. The method is shown to be independent of particle size, orientation and concentration, as well as image size and streak width.

In figure 2.3, the full line corresponds to $50l^+$, the dashed line to $70l^+$ and the symbols represent different aspect ratios, $r_p = 7$ ($\blacksquare$), $r_p = 14$ ($\blacktriangledown$), $r_p = 28$ ($\bullet$). The particle streak width, SW, found from the experiments are found to scale with l^+, as is the low speed velocity streaks in the fluid, see figure 2.3a, although there are clearly other effects to take into account. The fact that the particle streaks scale in the same manner as the low velocity streaks indicates that the fibres are located inside these low velocity structures. This is consistent with DNS of spherical particles, see *e.g.* Picciotto *et al.* (2005); Zhao *et al.* (2010), a feature believed to be due to the particle inertia.

Streakiness is a measure of the strength of particle streaks. For increasing Re_τ, the streakiness is observed to decrease, see figure 2.3b. Moreover, increasing Re_τ, also leads to decreasing the viscous length scale, l^+, meaning that the velocity structures decreases in size.

In each experiment, 150 images were captured, and with each image containing $150 - 1500$ fibres, a total of $22,500 - 225,000$ fibres were detected in each experiment. This large amount of fibres was seen to be enough for the fibre orientation data to converge. There are more measurement points in figure 2.3a than in figure 2.3b. The reason for this is that after the analysis method was developed, the streakiness did not converge for a few experiments, and those experiments are not included in the presented results.

CHAPTER 3

Orientation of Nano-Fibrillated Cellulose fibrils in laminar extensional flow

Nano-fibrillated cellulose, (NFC), is a new material with high potential in strength and stiffness, see Sakurada *et al.* (1962); Moon *et al.* (2011). With the decrease of newsprint there is an opportunity for one or several new high value forest-based products to enter the market. Studying the properties and behaviour of NFC is crucial in order to design the best possible application. In this section, the behaviour of a semi-dilute water/NFC dispersion in an extensional flow will be studied.

First, the concentration of elongated particles will be discussed, secondly the hydrodynamic focusing setup will be described and finally results of how small, light and elongated NFC particles behave in the accelerated flow will be presented.

3.1. Concentration aspects

Interactions between the different phases in a multiphase system of solids and liquids can be divided into different parts. The liquid will exert a force on the solid, and the solid will exert a force on the liquid. Furthermore, the solids can interact with each other either through hydrodynamic or mechanical forces. In a flowing suspension or dispersion the concentration of elongated particles is a key parameter when the dynamics of the flow are of interest. For low concentrations, the interactions between particles can be neglected and there are only fluid-particle interactions. The crowding number, N, defined as;

$$N = \frac{2}{3} C_v \left(\frac{l}{d} \right)^2 , \tag{3.1}$$

is used to quantify the number of mechanical interactions in a suspension containing elongated particles, reviewed by Kerekes (2006). The length of the particle is l, the diameter is d and the volume concentration is denoted C_v. Instead of considering the actual volume concentration, C_v, of all particles, the crowding number, N, relates the volume of the sphere that encloses the particle when swept over all angles to the total volume available. The crowding number, N, is the magnitude of the overlapping of these spheres, and hence the number of interactions between the particles when allowed to rotate freely.

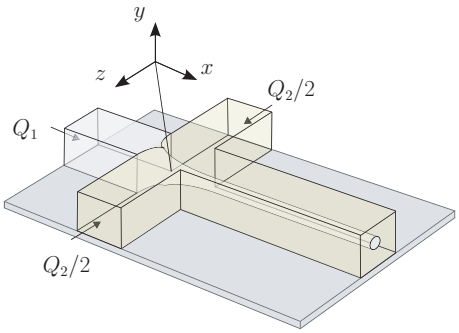

FIGURE 3.1. Schematic of the flow apparatus.

From the definition of N in equation 3.1, it should be noted that the aspect ratio, l/d is affecting N to the power of two, *i.e.* if the aspect ratio is large, particle-particle interactions can occur even at low volume concentrations.

There are three concentration regimes, (i) dilute $N << 1$, (ii) semi-dilute $1 < N < 60$ and (iii) concentrated $60 < N$, see Kerekes (2006). In the dilute regime, mechanical interactions between the particles seldom occur. However, even at low concentrations, hydrodynamic interactions may be of importance. In the semi-dilute regime, mechanical particle-particle interactions become substantial and when the suspension is concentrated, the particles movement are very restricted and a network is formed. Another commonly used quantity to define the concentration is nl^3, where n is the number of particles per volume. The crowding number is related to nl^3 as: $N = nl^3\pi/6$.

The most complex regime is the semi-dilute regime, where, depending on the size and shape of the particles, different behaviour are observed, Trevelyan & Mason (1951); Teraoka *et al.* (1985); Koch (1995). A comparison between experiments and computations in the semi-dilute regime are presented in the paper by Håkansson *et al.* (2012*b*).

3.2. Flow apparatus

The flow apparatus used in the paper by Håkansson *et al.* (2012*b*) is depicted in figure 3.1. There are three inlets and one outlet, where one liquid, with mass flow rate, Q_1, is focused by an outer sheath flow, with mass flow rate, Q_2, see figure 3.1. At the focusing point, where the four channels intersect, the inner core flow is accelerated and the flow is said to be extensional. This particular design was chosen partly due to its growing popularity in flow studies, see *e.g.* Knight *et al.* (1998); Anna *et al.* (2003); Cubaud & Mason (2006), but also because of its property of reducing the shear on the inner fluid. A generic setup is in this case wanted in order to validate the first results. Moreover, in this study the addition of particles in the flow are examined, which has not been

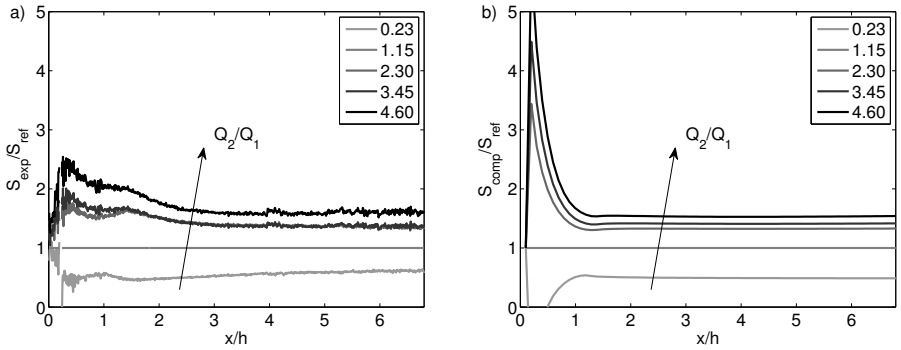

FIGURE 3.2. The relative order parameter S/S_{ref} versus downstream position, from the experiment (a) and the computation (b). The legend corresponds to Q_2/Q_1.

studied previously. The channel used here is one or two orders of magnitude greater in physical size compared to previous studies, making it possible to reach different parameter ranges.

The NFC dispersion shows a birefringent behaviour when the particles orientation distribution is anything but random. A solid or liquid is birefringent if it has different indices of refraction, depending on the incoming polarisation of the light. This property is utilized in order to measure the relative orientation in the flowing dispersion. The birefringence is observed as different light intensities when put between two crossed polarisers. The birefringent sample can rotate the polarisation of the light going through the first polariser and in this manner, light can pass through the second polariser, even though the polarisers are crossed. The magnitude of the rotation of the polarisation is dependent on the birefringence and the thickness of the sample. Moreover, the outgoing light intensity is periodic with respect to the rotation.

The sample is in this experiment the core flow, and since the intensity is periodically dependent on the thickness of the sample, a small sample is used to be sure that not more than half of a period is covered. This is one reason to why the same setup as in the previous chapter was not used. Another benefit with this setup is that the total sample volume is small, less than 10 ml of 0.3% NFC dispersion was used in this experiment compared to 120 l that is needed for the previous experiment.

3.3. Fibril orientation

In the paper by Håkansson *et al.* (2012*b*), both computations and experiments are performed in order to demonstrate that NFC fibrils align in the direction of the acceleration of an extensional flow. The size of the fibrils, with diameters

$\sim$ 40 nm and lengths of a few μm making them invisible to the human eye, and a birefringence based method was used to get a quantitative measure of the relative alignment. The NFC dispersion is fed into the core and accelerated by water from the sides, see figure 3.1. The acceleration, Q_2/Q_1, was varied and the orientation was observed; upstream of, during and downstream of the acceleration.

The Smoluchowski equation, Doi & Edwards (1986), was solved numerically for the orientation distribution at the centreline of the channel. A Brownian diffusion term and a flow acceleration term was included in the equation. The boundary conditions for the computations, *i.e.* the accelerations, were found through the experimental images, where the width of the NFC-dispersion thread at different positions could be detected. The thread was assumed to have a square cross section.

A relative order parameter, S/S_{ref}, was introduced and could be extracted from both the computations and experiments. The order parameter is a measure of how strong the alignment in a given direction is, here the flow direction is of interest (Håkansson *et al.* 2012*b*; van Gurp 1995). The case $Q_2/Q_1 = 1.15$ (closest to $Q_2/Q_1 = 1$) was used as reference, and in figure 3.2, the relative order parameter, S/S_{ref}, versus downstream position are shown. The fibrils are found to be more oriented for higher acceleration both in the experiments and in the computations. The computations show a much greater alignment during the acceleration, but both methods are of the same order in relative alignment further downstream.

CHAPTER 4

Discussion and future directions

4.1. Discussion

Non-spherical particles are a key ingredient in many kinds of materials, such as fibres in paper and polymers or fibrils in nano-scale materials. In the manufacturing processes of these materials, the design of the flow geometries are crucial and by introducing new designs, improved products can be made. In order to design better processes, the knowledge of the behaviour of non-spherical particles in different flow situations must be increased.

Cellulose based materials have been around for thousands of years and are here to stay. Cellulose is the world's most abundant polymer and is both biodegradable and renewable. Replacing oil-based materials with cellulose would be beneficial for the environment in many ways. Furthermore, the society would take a step towards a more sustainable future. These are a few reasons to why cellulose is the object of study in this thesis.

Two experiments were performed, where the first was a dilute suspension in a complex flow. The interactions between the flow and the particles were studied by observing the fibre orientation and position distributions. The orientation distribution of sedimenting fibres towards a wall in a turbulent shear flow is far from simple to predict. The fibres are affected by many competing forces, such as sedimentation, wall interactions, turbulence, shear, inertia. In this study, it was concluded that sedimentation, wall interactions and the fluid interia where the dominant forces in the parameter region studied. Through the analysis of the position distributions of the fibres, it was found that the fluid structures forced the fibres to agglomerate in fibre streaks. As the fluid structures became smaller, so did the tendency for the fibres to agglomerate in streaks.

The knowledge gained through the first experiments can not only be of interest to the papermaking process, it can also be used to validate numerical simulations. The distinct difference between the orientations distribution of the short fibres and the long fibres is a challenging validation case for simulations.

It was shown in the second experiment, where a semi-dilute NFC dispersion was accelerated by a sheath flow, that the small elongated particles aligned and stayed aligned, in the flow direction. A numerical computation was performed

with confirming results. These results are very interesting when designing new processes where the alignment and structure of the material is important. The alignment of the particles is expected, but the speed of randomisation due to Brownian diffusion is difficult to predict. The particle-particle interactions are believed to help the fibrils stay aligned, and this system should therefore be highly concentration dependent. A much higher concentration on the other hand, may not align at all, due to the formation of networks at the inlet.

Contractions and extensional flows are widely used in order to align elongated particles. But in a confined converging geometry, the flow is not only extensional, shear forces are strong close to the walls and the shear is affecting the final orientation distribution. In the present setup, the sheath flow acts as a lubricant, and hence minimises the shear on the core flow. The shear is believed to make the orientation distribution more random compared to a pure extensional flow, and as seen in the first experiment, shear can give rise to unwanted flow structures.

4.2. Future directions

In order to design or improve a process, the physics behind the process needs to be known. The turbulent channel experiment showed that elongated particles gathered in streamwise structures, and the reason is suggested to be related to the flow structures. Therefore one way of achieving a more homogeneous distribution would be to remove the flow structures. Future work on this experiment could be focused on determining where in the wall normal direction the fibres are located, and perform combined flow and particle velocity measurements. However, these experiments will not be pursued by the author.

The future work will be carried out in order to obtain a better understanding as well as improving the flow focusing setup. Achieving a higher degree of alignment, and measuring how long the alignment lasts, is one direction. This could be achieved with an increased speed, that in turn would eventually lead to hydrodynamic instabilities. The geometry can also be changed in order to achieve a higher degree of alignment. The numerical calculations could also be used to predict the behaviour in a different geometry and in a dispersion of higher concentration. The numerical model will be improved by including a more realistic velocity profile.

Another direction is to include chemistry in the channels. Diffusing particles or polymers through the interfaces would be of interest in a possible composite process.

A third future direction is aiming on orienting fibrils in a sheet instead of in a thread. A 2-dimensional system will of course be more complex, and the design of the setup is at this point not clear. However, orienting particles with a sheath flow in a similar manner should be possible, and would be of great interest.

Finding a quantitative comparison between a pure extensional flow and an extensional flow with shear is an intriguing project. An experiment would be preferred, but the manufacturing of such a 3-dimensional channel is not trivial.

CHAPTER 5

Papers and authors contributions

Paper 1

Measurement of width and streakiness of particle streaks in turbulent flows
K. Håkansson (KH), M. Kvick (MK), F. Lundell (FL), L. Prahl Wittberg (LPW) & L. D. Söderberg (DS). To be submitted

A new method for quantification of particle streaks is developed. KH and MK developed the method and performed the analysis under supervision of FL, LPW and DS. KH investigated and accounted for the dependence of concentration, image size, artificial particle size and streak width in the method. MK incorporated the Voronoi method into the analysis. KH, MK, FL and LPW wrote the paper jointly with input from DS.

Paper 2

Fibre orientation and fibre streaks in turbulent wall bounded flow
M. Kvick (MK), K. Håkansson (KH), F. Lundell (FL), L. Prahl Wittberg (LPW) & L. D. Söderberg (DS). To be submitted

The orientation and spatial distribution of fibres in a turbulent wall bounded flow is studied experimentally. MK and KH performed a majority of the experiments and analysis in close collaboration under supervision of FL, LPW and DS. In addition, KH performed the LDV measurements and MK implemented the anisotropy as an analysis method. MK, KH, FL and LPW wrote the paper jointly with input from DS. Parts of these results have been published in:

> *Streak Formation and Fibre Orientation in Near Wall Turbulent Fibre Suspension Flow*
> M. Kvick, K. Håkansson, F. Lundell, L. D. Söderberg & L. Prahl Wittberg
> **ERCOFTAC bulletin, 2010, Vol. 84**

Fibre Streaks in Wall Bounded Turbulent Flow
M. Kvick, K. Håkansson, F. Lundell, L. D. Söderberg & L. Prahl Wittberg
7$^{\text{th}}$ Int. Conf. on Multiphase Flow
May 30 – June 4 2010, *Tampa, FL, USA*

Paper 3

Orientation of nano-fibrillated cellulose in accelerated flow
K. Håkansson (KH), F. Lundell (FL), L. Prahl Wittberg (LPW), L. Wågberg (LW) & L. D. Söderberg (DS). Manuscript in preparation

This work is a combination of experiments and simulations, were the experiments were conducted by KH. The numerical code was written by FL and KH, while the simulations were performed by KH. The data analysis was performed by KH with input from FL and the writing was performed by KH with input from FL, LPW, LW and DS. The original idea for the work was suggested by FL, LW and DS.

Acknowledgements

The Knut and Alice Wallenberg Foundation is greatly acknowledged for funding the Wallenberg Wood Science Center, in which this work has been carried out.

A big thank you goes to my three supervisors, first of all Daniel Söderberg for accepting me as a PhD student and for all the great ideas and deeper questions, second of all Fredrik Lundell for the every day guidance, motivation and support at all times. Last but not least Lisa Prahl Wittberg for the large amounts of proof reading and the discussions, enhancing my understanding of the underlying concepts.

I would also like to give a special thanks to Mathias, with whom I spent many long days in the basement. It would have taken more than twice as long to do everything without you and it would not have been half as fun.

Thank you Andreas Fall, for introducing me to colloidal chemistry (more than once), the thoughtful discussions and also for providing clean NFC samples.

I am very happy to a part of the paper group, where Outi has taught me lots about stability, Allan helped with tips and insights regarding the water table, and Gabri always had good ideas on more general experimental and multiphase problems. Tomas, Michail, Afshin, Ramin, Charlotte, Gustav, Roland and Yu who are or have been a part of the group since I started, are thanked for the pleasant working environment.

Kim and Göran in the workshop is greatly thanked for always helping out and being in a good mood. Christian Aulin, Tom Lindström and Innventia AB are greatly acknowledged for providing the NFC. I would like to thank Lars Wågberg for all great insights, ideas and proposals. Thanks to Dr. Mihai Mihaescu for reviewing this thesis.

The people at the fluid physics laboratory deserves a mentioning for the nice work place atmosphere and the fikas. Thank you Olle, Alexander, Ramis, Antonio, Sissy, Shintaro, Markus, Julie, Alexandre, Renzo, Sohrab, Niklas, Robert, Martin, Johan, Emma, Ylva, Shahab, Bengt, Fredrik, Malte and Thomas. I

would also like to thank the people at OB18, especially: Peter, Marit, Johan, Florian, Enrico, Andreas, Qiang, Daniel, Stevin and Feng.

Everyone in the WWSC both from KTH and Chalmers, are greatly acknowledged for the good times at the workshops and during the doctoral courses.

Karl Håkansson

References

Anna, S., Bontoux, N. & Stone, H. A. 2003 Formation of dispersions using "flow focusing" in microchannels. *Applied Physics Letters* **82** (3), 364–366.

Carlsson, A. 2009 Near wall fibre orientation in flowing suspensions. PhD thesis, KTH Mechanics, Royal Institute of Technology.

Carlsson, A., Håkansson, K., Kvick, M., Lundell, F. & Söderberg, L. D. 2011 Evaluation of steerable filter for detection of fibers in flowing suspensions. *Exp in Fluids* **51**, 987–996.

Carlsson, A., Lundell, F. & Söderberg, L. D. 2007 Fiber orientation control related to papermaking. *Journal of Fluids Engineering* **129** (4), 457–465.

Cox, H. L. 1952 The elasticity and strength of paper and other fibrous materials. *British Journal of Applied Physics* **3** (3), 72.

Cubaud, T. & Mason, T. 2006 Folding of viscous threads in diverging microchannels. *Physical review letters* **96** (11), 114501.

Doi, M. & Edwards, S. 1986 *The theory of polymer dynamics*. Oxford University Press Inc.

Eichhorn, S. J., Dufresne, A., Aranguren, M., Marcovich, N. E., Capadona, J. R., Rowan, S. J., Weder, C., Thielemans, W., Roman, M., Renneckar, S., Gindl, W., Veigel, S., Keckes, J., Yano, H., Abe, K., Nogi, M., Nakagaito, A. N., Mangalam, A., Simonsen, J., Benight, A. S., Bismarck, A., Berglund, L. A. & Peijs, T. 2010 Review: current international research into cellulose nanofibres and nanocomposites. *J Mater Sci* **45** (1), 1–33.

van Gurp, M. 1995 The use of rotation matrices in the mathematical description of molecular orientations in polymers. *Colloid Polym Sci* **273**, pp. 607–625.

Håkansson, K., Kvick, M., Lundell, F., Prahl Wittberg, L. & Söderberg, L. D. 2012*a* Measurement of width and amplitude of particle streaks in turbulent flows. To be submitted.

Håkansson, K., Lundell, F., Prahl Wittberg, L., Wågberg, L. & Söderberg, L. D. 2012*b* Orientation of nano-fibrillated cellulose in accelerated flow. Manuscript in preparation.

Jeffery, G. B. 1922 The motion of ellipsoidal particles immersed in a viscous fluid. *Proceedings of the Royal Society of London. Series A, Containing Papers of a Mathematical and Physical Character* **102** (715), pp. 161–179.

Jeong, J., Hussain, F., Schoppa, W. & Kim, J. 1997 Coherent structures near the wall in a turbulent channel flow. *Journal of Fluid Mechanics* **332**, 185–214.

Kerekes, R. J. 2006 Rheology of fibre suspensions in papermaking: An overview of recent research. *Nordic Pulp and Paper Research Journal* **21** (5), 598–612.

Kim, J., Moin, P. & Moser, R. 1987 Turbulence statistics in fully developed channel flow at low reynolds number. *Journal of Fluid Mechanics* **177** (1), 133–166.

Knight, J. B., Vishwanath, A., Brody, J. P. & Austin, R. H. 1998 Hydrodynamic focusing on a silicon chip: mixing nanoliters in microseconds. *Phys. Rev. Lett.* **80** (17), 3863–3866.

Koch, D. L. 1995 A model for orientational diffusion in fiber suspensions. *Phys. Fluids* **7**, 2086–2088.

Kvick, M., Håkansson, K., Lundell, F., Prahl Wittberg, L. & Söderberg, L. D. 2012 Fibre orientation and fibre streaks in turbulent half channel flow. To be submitted .

Lagraa, B., Labraga, L. & Mazouz, A. 2004 Characterization of low-speed streaks in the near-wall region of a turbulent boundary layer. *European J Mech - B/Fluids* **23** (4), 587 – 599.

Lundell, F., Söderberg, L. D. & Alfredsson, P. H. 2011 Fluid mechanics of papermaking. *Annual Review of Fluid Mechanics* **43** (1), 195–217.

Matsubara, M. & Alfredsson, P. H. 2001 Disturbance growth in boundary layers subjected to free-stream turbulence. *J. Fluid Mech.* **430**, pp. 149–168.

Moon, R. J., Martini, A., Nairn, J., Simonsen, J. & Youngblood, J. 2011 Cellulose nanomaterials review: structure, properties and nanocomposites. *Chem. Soc. Rev.* **40** (7), 3941.

Morton, W. & Hearle, J. 1975 *Physical properties of textile*. London: William Heinemann Ltd.

Norman, B., Salmen, L., Annergren, G., Hagen, N., Stenström, S., Wikström, M., Engström, G. & Ström, G. 2005 *The Ljungberg Textbook, Paper Processes*. Fibre and Polymer Technology, KTH.

Pääkkö, M., Ankerfors, M., Kosonen, H., Nykänen, A., Ahola, S., Österberg, M., Ruokolainen, J., Laine, J., Larsson, P. T., Ikkala, O. & Lindström, T. 2007 Enzymatic hydrolysis combined with mechanical shearing and high-pressure homogenization for nanoscale cellulose fibrils and strong gels. *Biomacromolecules* **8**, pp. 1934–1941.

Picciotto, M., Marchioli, C. & Soldati, A. 2005 Characterization of near-wall accumulation regions for inertial particles in turbulent boundary layers. *Phys. Fluids* **17**, 098101.

Sakurada, I., Nubushina, Y. & Ito, T. 1962 Experimental determination of the elastic modulus of crystalline regions in oriented polymers. *J Polymer Sci* **57**, 651–660.

Teraoka, I., Ookubo, N. & Hayakawa, R. 1985 Molecular theory on the entanglement effect of rodlike polymers. *Phys Rev Lett* **55**, pp. 2712–2715.

Trevelyan, B. J. & Mason, S. G. 1951 Particle motions in sheared suspensions. i. rotations. *J of Colloid Sci* pp. 354–367.

Zacksenhouse, M., Abramovich, G. & Hetsroni, G. 2001 Automatic spatial

characterization of low-speed streaks from thermal images. *Experiments in Fluids* **31** (2), 229–239.

Zhao, L. H., Andersson, H. I. & Gillissen, J. J. J. 2010 Turbulence modulation and drag reduction by spherical particles. *Physics of Fluids* **22** (8), 081702.

Part II

Papers

1

Paper 1

Measurement of width and streakiness of particle streaks in turbulent flows

By Karl Håkansson, Mathias Kvick, Fredrik Lundell, Lisa Prahl Wittberg & L. Daniel Söderberg

Wallenberg Wood Science Center & Linné Flow Centre, KTH Mechanics, Royal Institute of Technology, SE – 100 44 Stockholm, Sweden

To be submitted

Fibre streaks are observed in experiments with fibre suspensions in a turbulent half channel flow. The preferential-concentration method, most commonly used to quantify preferential particle concentration, is found to break down at low concentrations.

Two different new streak quantification methods are evaluated, one based on Voronoi analysis and the other based on artificial particles with an assigned fixed width. The width of the particle streaks, and a measure of the intensity of the streaks, *i.e.* streakiness, are sought. Both methods are based on the auto-correlation of a signal, generated by summing images in the direction of the streaks. Common for both methods is a severe concentration dependency, verified in experiments keeping the flow conditions constant while the (very dilute) concentration of fibres is altered.

The fixed width method is shown to be the most suitable method, being more robust and less computationally expensive. By assuming the concentration dependence to be related to random noise, an expression is derived, that is shown to make the streak width and the streakiness independent of the concentration even at as low concentrations as 0.05 particles per column in an image. The streakiness is obtained by applying an artificial particle width equal to 20% of the streak width. This width is in this study found to be large enough to smoothen the correlation without altering the streakiness nor the streak width. It is concluded that in order to make quantitative comparisons between different experiments or simulations, the evaluation has to be performed with care and be very well documented.

---

1. Introduction

When introducing particles into a turbulent wall bound-ed flow, it is well known that the particles tend to agglomerate into streamwise streaks close to the walls. This has been found both in experiments, *e.g.* (Rashidi *et al.* 1990; Fessler *et al.*

1994; Kulick *et al.* 1994; Kaftori *et al.* 1995*a*,*b*; Ninto & Garcia 1996), and in simulations, *e.g.* (Pedinotti *et al.* 1992; Rouson & Eaton 2001; Narayanan *et al.* 2003; Marchioli *et al.* 2010).

In many industry processes, *e.g.* paper making, particle suspensions are pumped and transported through different geometries at high speeds, resulting in turbulent wall bounded flows. In order to understand how the particles are influenced by the turbulent flow, it is important to obtain a quantitative measure of the strength of the tendency for the particles to agglomerate into streaks. This is also necessary if different experiments and simulations are to be compared.

Even though several methods exist to investigate clustering, these methods are not able to provide information whether particles form streaks or not.

Fessler *et al.* (1994) introduced the parameter D, quantifying 2-dimensional preferential concentration, defined by comparing the measured particle density to a random distribution:

$$D = \frac{\sigma - \sigma_p}{\lambda} \tag{1}$$

where σ is the standard deviation of the measured particle density, σ_p is the standard deviation of a random Poisson distribution and λ is the mean particle density. D becomes positive if clusters and voids are present, negative if the particle distribution is homogeneous and zero if the particles are randomly distributed. The parameter D is dependent of the box size, and by finding the box size that maximizes D, the typical cluster size can be found.

A more recent preferential concentration quantification method, based on Voronoi analysis, was proposed by Monchaux *et al.* (2010). In a Voronoi analysis, each particle is assigned a cell with an area inversely proportional to the local concentration. Comparing measured cell areas to a Poisson distribution provides the location and characterization of clusters.

The preferential concentration parameter D will be shown to be concentration dependent and thus failing to provide a consistent measure of the typical cluster size. The Voronoi analysis method displays a similar behavior. Therefore, in order to characterize the 1-dimensional streaks, more information is needed, emphasizing the need of a new method.

In this article, correlations in the spanwise direction, normal to the streaks, will be used to determine (i) a streak width and (ii) an objective quantification of the qualitative term "streakiness" (tendency to agglomerate in streaks). This correlation will be obtained in two ways, both of which make use of the position of individual particles in an image. The first is based on a Voronoi analysis; the second is a straightforward correlation similar to a sum of image intensities. The second method is determined to be most suitable. As a result a scheme to determine the streak width and the streakiness independent of particle size, orientation, concentration, image size and streak width is obtained, including a consistent way of setting the one input parameter. The dependence of:

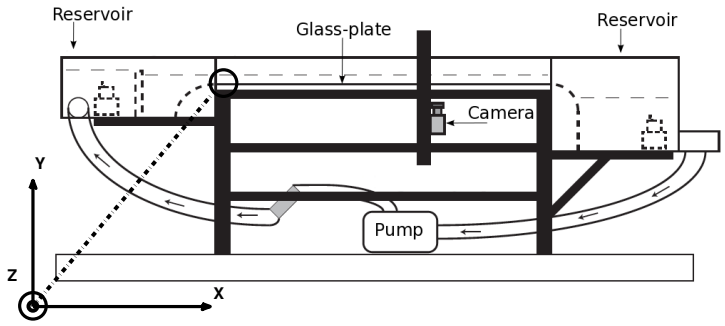

FIGURE 1. Schematic of the flow apparatus

- particle size and orientation is treated by identifying the center of gravity of the particles in the images.
- concentration effects on the correlation is treated using the correlation from an image with randomly placed particles.
- image size is treated by considering the finite length of the input signal into the correlation.
- streak width is treated by normalizing the input parameter with the streak width (iterations are needed).

2. Methods

2.1. *Flow apparatus*

Images of a fibre suspension in a turbulent half channel flow have been acquired. Fig. 1 depicts the flow apparatus where the suspension is pumped from a downstream to an upstream reservoir, allowing the suspension to flow down an inclined glass plate. A camera is mounted underneath the glass plate acquiring images of the fibres in the flow. A typical image is shown in Fig. 2, showing clearly that fibres form streaks. Pumps are placed in the upstream and downstream reservoirs in order to stir the suspension, and prevent fibres from sedimenting in the reservoirs. The coordinate system is defined so that the x-axis correspond to the streamwise direction, the y-axis is in the wall normal direction and the z-axis is in the spanwise direction. The origin is positioned on the leading edge of the glass plate with $z = 0$ on its centreline.

Velocity profiles of the flow were measured with Laser Doppler Velocimetry (LDV) at the acquisition point, upstream of the acquisition point and also at two spanwise positions. The velocity profiles showed good agreement with DNS data for a full channel and the flow was confirmed to be turbulent and fully developed. More details regarding the setup and the LDV measurements can be found in Kvick *et al.* (2012), where the same setup was used.

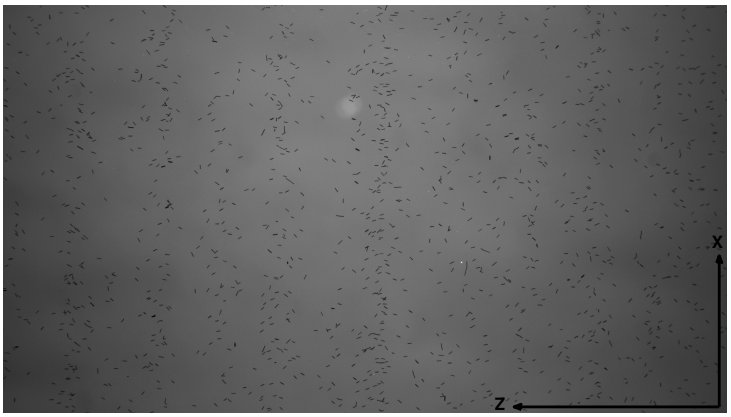

FIGURE 2. Example of an image from a turbulent fibre suspension flow with clear fibre streaks. The fibres are black, the differences in intensity are mostly due to the focusing of the light source, the flow is from bottom to top

Since the flow is driven by gravity alone, the wall shear stress, τ_w, can be calculated through the force balance at the wall;

$$\tau_w = \rho g h \sin\alpha. \tag{2}$$

Here ρ represents the density of the fluid, g is the gravitational acceleration, h is the height of the water layer on the glass plate and α is the inclination angle of the plate. The friction Reynolds number is defined as;

$$Re_\tau = \frac{h u_\tau}{\nu} = \frac{h\sqrt{gh\sin\alpha}}{\nu}, \tag{3}$$

where $u_\tau = \sqrt{\tau_w/\rho}$ and ν represent the friction velocity and the kinematic viscosity, respectively.

The suspension consists of water and cellulose acetate fibres with density 1300 kg/m^3 and concentrations $nl^3 = 0.0007 - 0.006$. For each case, 150 statistically independent images (1920×1080 pixels) are acquired, *i.e.* all fibres are transported out of the field of view of the camera before the next image is taken.

The positions of the fibres in the images are obtained by the use of a steerable filter, described in Carlsson *et al.* (2011). Using this filter, it is possible to detect both fibre positions and orientations in the flow-vorticity plane. The filter can even detect crossed fibres to a certain degree. Several layers of fibres or fibres covering most of the image can not be identified by the filter. This is one of the reasons to why the experiment has to be performed at low concentrations of fibres in the suspension. With index of refraction matching methods (where a

TABLE 1. Table of experiments with different concentration of fibres.

Case	Re_τ	r_p	c	Physical conc.	Artificial conc.
1	110	7	0.12	●	○
2	110	7	0.46	■	□
3	110	7	0.55	◀	◁
4	110	7	0.75	▶	▷
5	110	7	0.97	▼	▽

only a fraction of the actual particles are visible), higher particle concentrations can be reached. However, the concentration of visible particles would still be limited, since the detection is dependent of the resolution of the camera and the size of the particles.

To evaluate the different analysis methods, the experiments are performed using constant Re_τ and aspect ratio, but different fibre concentrations. This is referred to as physical concentration in this study. An artificial concentration variation is also used, by detecting and identifying all fibres in the images, and randomly excluding fibres during post processing. Note that aspects such as streakiness and streak width should be constant during the artificial concentration variation, since the fibres are removed randomly.

Firstly, five experiments at $Re_\tau = 110$, with fibres of aspect ratio $r_p = 7$ and varying fibre concentration will be considered. The particle (fibre) concentration, c, are measured in particles (fibres) per column of pixels in the image. The specifications for the five cases are displayed in table 1. Case 3, where clear streaks are observed, will be used as an example to illustrate differences in the two new analysis methods. Thereafter quantitative results from five other cases ($\mathrm{Re}_\tau = 51 - 178$) will be shown in order to highlight differences in streakiness. Finally the experiments with different concentration will be considered.

2.2. *Preferential concentration parameter, D*

The preferential concentration parameter, D, defined in equation 1, is in this 1-dimensional case calculated using columns in the direction of the streaks instead of boxes. The width of the columns are varied and the resulting values of D are displayed in Fig. 3. Fig. 3 shows cases 1-5 where only the concentration has been varied, $0.12 < c < 0.97$ particles per column. It can be concluded that D is concentration dependent, and the jagged appearance of the curves makes it difficult to determine what a typical streak size would be. In this kind of flow the streaks are expected to appear at random streamwise positions, but having a similar size (width), as the case for low and high velocity streaks in e.g. Lagraa *et al.* (2004). Due to the concentration dependence and the many peaks of the D-curves in Fig. 3, further development of the method is needed, or a new approach needs to be developed. The latter is pursued in this study.

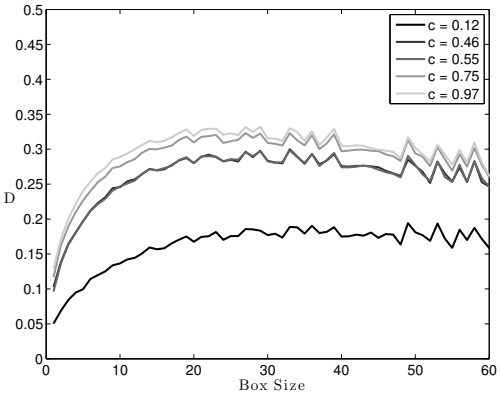

FIGURE 3. The preferential concentration parameter, D, versus box size in pixels

2.3. *Correlation based analysis*

The analysis methods presented in this paper are based on auto-correlating a discrete signal obtained from an image, the correlation curves are used to quantify the streaks. The signal is denoted, I, and the auto-correlation of the signal, R_{II}, is defined as:

$$\hat{R}_{II}(\Delta z) = \int I(z + \Delta z) I(z) dz, \quad R_{II} = \frac{\hat{R}_{II}}{\max \hat{R}_{II}}. \tag{4}$$

The signal used in the correlations are obtained in different manners by the two different methods. However, the basic idea is the same: summing intensities in the direction along the streaks. A straightforward way of obtaining the signal is to sum the intensities of the raw images in the streaky direction. This is similar to standard investigations of high and low velocity streaks in turbulent or transitional boundary layers, see *e.g.* Lagraa *et al.* (2004) or Fransson & Alfredsson (2003). In this way, information regarding the sizes and strengths of the structures can be extracted fairly easy.

However, using raw images as input into the analysis, several problems arises. One is the effect of differences in light intensities in the image. Another important aspect is the influence of the particle orientation in case of non-spherical particles. The signal will have a very different appearance depending on if the particles are oriented in the summing direction or perpendicular to it. To be able to assess these problems, it is necessary to use only the particle positions, and thereby reducing the number of non-controllable parameters.

The position and orientation of each particle are found in a first post processing step as mentioned earlier. With the positions known, the control over

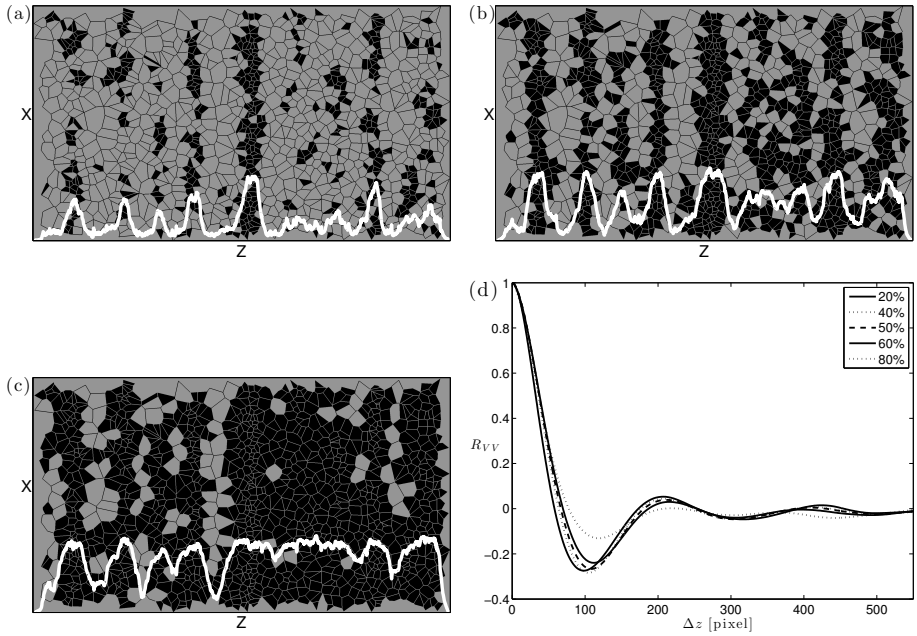

FIGURE 4. Voronoi map of the image in Fig. 2 with threshold (a) 20%, (b) 50% and (c) 80%, considered clustered with a high local density and here colored black, the resulting signal for each image is colored white. (d) R_{VV} for the complete set. The percentages in the legend corresponds to the part of the images considered to belong to streaky regions, and therefore contributing to the signal

the input into the analysis is very high and comparable to the data from Lagrangian simulations.

2.4. *Correlations based on Voronoi analysis*

In order to obtain an analysis method independent of particle width and orientation, a Voronoi tessellation is applied to the particle positions. In a Voronoi diagram, the image is divided into an unstructured grid with one particle in each cell. The size and shape of each cell is determined by the surrounding particles. Particles located in regions with high local concentration has small cell areas and particles in regions were the concentration is lower has larger cell areas.

Thresholding the distribution of cell areas makes it possible to control the cells that are to be regarded as clustered and located in streaks, corresponding

to small areas. Assigning a value, *e.g.* 1, to the small areas and summing the image in the streamwise direction results in a signal that can be auto-correlated.

Fig. 4a–4c shows different thresholds for a Voronoi diagram based on Fig. 2, together with the resulting signals. In Figs. 4a–4c, 20%, 50% and 80% of the total image area is regarded as clustered cells, respectively. The clustered cells are colored black (value 1), and a summation of the images in the streaky direction (vertical) results in the signals displayed in white.

The signals are auto-correlated and the mean of the auto-correlations for all 150 images in the measurement set is displayed in Fig. 4d. The Voronoi based correlations, denoted R_{VV}, vary for different thresholds but display a lowest minimum for a threshold close to 50%. 50% is used as the threshold value in the rest of this paper. There are other options to threshold. For example, use the deviation of a random distribution of cell areas as the threshold, see *e.g.* Monchaux *et al.* (2010). Due to the low concentrations used in the present study, the thresholds were inconsistent.

2.5. *Correlations based on a fixed width*

The second method uses the positions of the physical particles to construct images with artificial particles.

In order to smoothen the signal, the width, w, of the artificial particles is fixed to a value larger than one pixel. In Fig. 5a - 5c, three choices of particle widths are shown, based on the image in Fig 2. The sums of these artificial images are shown in black and, as is evident, the particle width influences the signal. Furthermore, as can be seen in Fig. 5d showing the correlation R_{ff} for the different particle widths, the choice of particle width plays an important role for the resulting correlation and must not be greater than the streak width. A particle width larger than the streak width results in that the small peaks are filtered out. In Fig. 5d it is noted that the correlations first zero crossing does not change significantly until the particle fixed width exceeds 41 pixels.

2.6. *Determination of streak width,* $2\Delta z(R_{II} = 0)$*, and streakiness,* $\Xi(R_{II})$*, from correlations*

The streak width is in this study determined as the displacement at which the minimum correlation occurs. However, this point is never well defined. Therefore the first zero-crossing, that can be interpolated, is taken as the streak half width, $\Delta z(R_{II} = 0)$, where $R_{II} = 0$ implies the first position at which the correlation is zero. The same approach was used for velocity streaks by Fransson & Alfredsson (2003) and shown to be consistent.

The minimum value of the correlation is a measure of how coherent the particle structures are, *i.e.* a measure of the strength of the streaks. The streakiness is from here on defined as; $\Xi(R_{II}) = |min(R_{II})|$. A lower negative

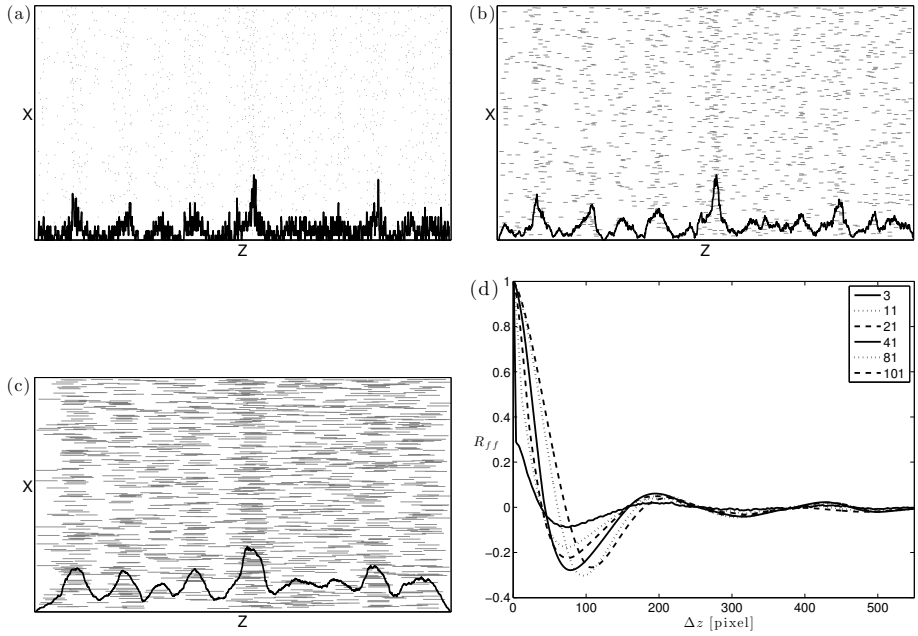

FIGURE 5. Determination of horizontal correlation using particle position from the image in Fig. 2. (a) Image with fixed particle width $w = 3$ pixel and vertical sum of this figure, (b) image with fixed particle width $w = 21$ pixels and vertical sum of this figure, (c) image with fixed particle width $w = 101$ pixels and vertical sum of this figure, (d) correlations for $w = 3, ..., 101$ pixels

minimum value of the correlation implies higher or stronger streakiness. In other words that the particle structures in the flow are more coherent.

3. Results and Discussion

3.1. *Fixed width vs. Voronoi based correlation*

In Fig. 6, the correlation of the Voronoi based analysis with a threshold of 50% is depicted together with the correlation using the fixed width method with a particle width of 21 pixels. It can be seen that the Voronoi based method gives a lower minimum and is shifted to the right. The reason for the shift of the correlation curve will be shown to be due to the concentration dependency. An evaluation of the concentration dependency of both methods, and a solution in order to obtain the streakiness and streak width independent of concentration is described below.

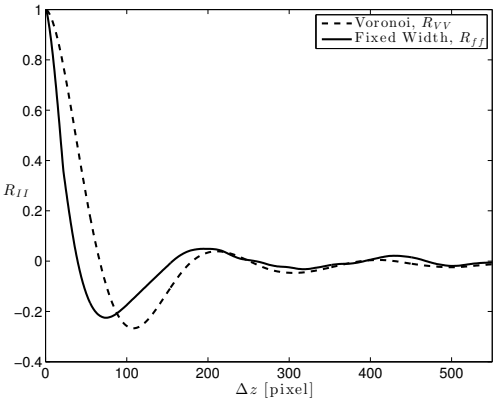

FIGURE 6. Comparison of the Voronoi based correlation, R_{VV}, and the fixed width based correlation, R_{ff}, where the fixed width has been set to 21 pixels and the threshold in the Voronoi analysis to 50%

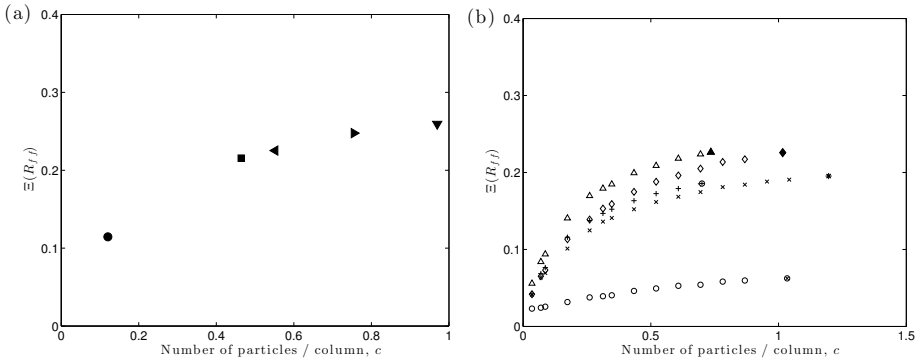

FIGURE 7. Streakiness as a function of concentration using (a) experimental and (b) artificial variation. In (b) several cases corresponding to different Reynolds numbers and concentrations are shown, $(\otimes, *, \oplus, \blacklozenge, \blacktriangle)$ is the original concentration and $(\circ, \times, +, \diamond, \triangle)$ are the artificial variations. Each symbol pair belongs to one experimental case. The fixed width method was used in both (a) and (b)

3.2. *Effect of number of particles*

3.2a. *Streakiness,* $\Xi(R_{II})$. The number of particles in each image (concentration) affects the analysis independently of the method used. Since experimental images will have a fairly low concentration (even if index-of-refraction has been

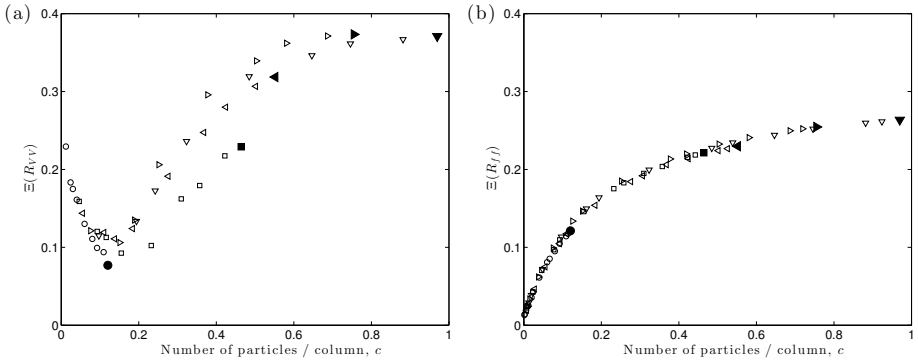

FIGURE 8. Scaling of streakiness for different number of particles, both physical ($\bullet, \blacksquare, \blacktriangleleft, \blacktriangleright, \blacktriangledown$) and artificial ($\circ, \square, \triangleleft, \triangleright, \triangledown$) concentration variations, (a) using Voronoi based correlation and (b) using fixed width correlation

used and the actual concentration is quite high), the method needs to be able to handle low concentrations. In order to investigate how the concentration affects the outcome of the different analysis methods, experiments with different concentrations of particles in the suspension were performed, while the flow conditions were kept constant.

The other way of changing the concentration is random removal of particles from the pictures during post processing. In Fig. 7a and 7b, the streakiness, $\Xi(R_{ff})$, versus the number of particles per column, c, are shown, using the fixed width method. Fig. 7a depicts results from a physical concentration variation and 7b the artificial concentration variations for five different flow cases. The symbols ($\otimes, *, \oplus, \blacklozenge, \blacktriangle$) represent the original measurements in 7b and the symbols ($\circ, \times, +, \diamond, \triangle$) represent the artificial variations of concentration, where the Reynolds' numbers used are $\mathrm{Re}_\tau = 51, 178, 167, 71$ and 88, respectively. The different experiments have different concentrations and different streakiness.

In Fig. 8a the Voronoi based method is used and both physical, ($\bullet, \blacksquare, \blacktriangleleft, \blacktriangleright, \blacktriangledown$), and artificial, ($\circ, \square, \triangleleft, \triangleright, \triangledown$), concentration variations are performed. The similarity between the two different concentration variations using the Voronoi method is poor. In Fig. 8b it is shown that by excluding particles in the post processing it is possible to recreate the behavior observed in the experiments using the fixed width method. Note that a naive interpretation of the data in Fig. 7a is that the streakiness varies with concentration, whereas Fig. 8b shows that this variation is an artifact of the evaluation. In section 3.3, corrections for this artifacts are derived and demonstrated to give a consistent quantification of the streakiness.

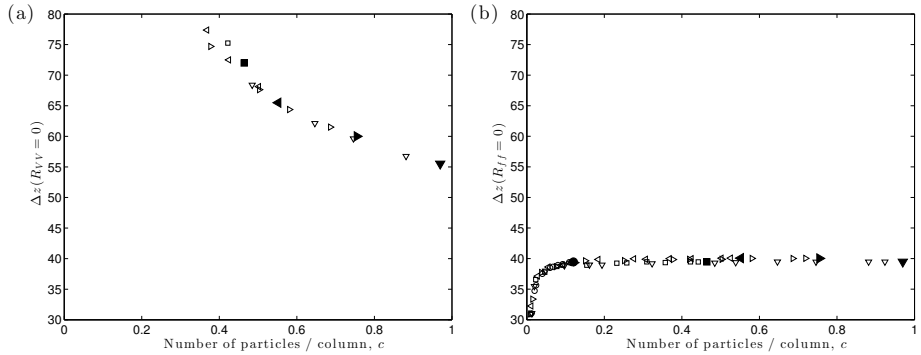

FIGURE 9. Streak width for different number of particles, both physical ($\bullet, \blacksquare, \blacktriangleleft, \blacktriangleright, \blacktriangledown$) and artificial ($\circ, \square, \triangleleft, \triangleright, \triangledown$) concentration variations, (a) using Voronoi based correlation and (b) using fixed width correlation

3.2b. *Streak width,* $2\Delta z(R_{II} = 0)$. Fig. 9 shows both physical ($\bullet, \blacksquare, \blacktriangleleft, \blacktriangleright, \blacktriangledown$) and artificial ($\circ, \square, \triangleleft, \triangleright, \triangledown$) concentration variations of the streak half width in pixels. The Voronoi based method and the fixed with method are displayed in Fig. 9a and 9b, respectively. The fixed width method has a stable streak width for concentrations greater than ~ 0.1 particles per column. The Voronoi method on the other hand display a significant variation in streak width, explaining the shift of the Voronoi correlation curve as shown in 6. The behavior of the Voronoi analysis is logic; less particles leads to a larger average cell size, resulting in a larger streak width.

3.3. *Obtaining a consistent measure*

When comparing the two methods, three major advantages can be found for the fixed width method: (i) the streak width is independent of the concentration, (ii) the collapse of the physical and artificial concentration variation is better and (iii) it is computationally cheaper as compared to the Voronoi based method. Due to the above mentioned advantages, the fixed width method is the approach that will be considered and improved so that consistent measures are obtained. The aspects that needs to be taken into account are concentration, and the artificial particle width w. The latter needs to be considered in relation to the actual streak width why an iteration will be needed in order to find w.

In order to determine the relative streakiness, the particles are first located and given a width, the image is summed in the streak direction to obtain the signal. Thereafter, the auto-correlation is computed using the resulting signal. If the concentration between the measurements is not constant, this needs to

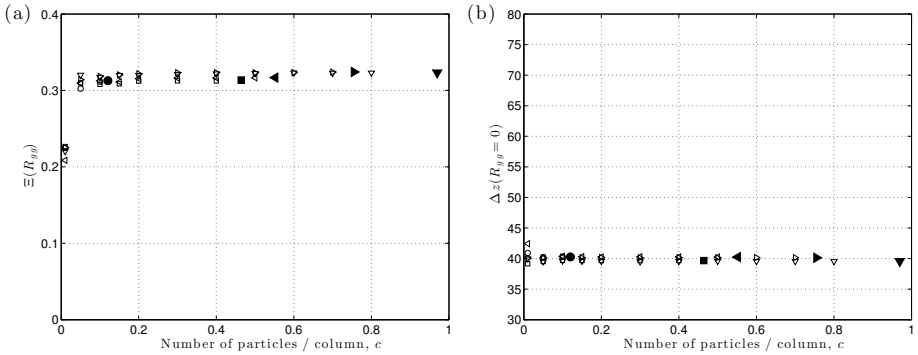

FIGURE 10. (a) Streakiness and (b) streak widths for different number of particles, both physical ($\bullet, \blacksquare, \blacktriangleleft, \blacktriangleright, \blacktriangledown$) and artificial ($\circ, \square, \triangleleft, \triangleright, \triangledown$) concentration variations, from the true correlation R_{gg} (equation 7)

be taken into account. Note that this implies that the procedure below has to be applied before concentration effects of streakiness are deduced.

3.3a. *Concentration.* The concentration dependence is reduced by first assuming that the signal $I = f(z, c)$ consists of a true signal $g(z, c)$ and a perturbation $g'(z, c)$, both dependent on the concentration $c \in [0, \infty]$, as;

$$f(z, c) = g(z, c) + g'(z, c). \tag{5}$$

The auto-correlation $\hat{R}_{ff}(\Delta z, c)$ can be split into three parts;

$$\begin{aligned} &\hat{R}_{ff}(\Delta z, c) = \\ &\quad = \hat{R}_{gg}(\Delta z, c) + \hat{R}_{gg'}(\Delta z, c) + \hat{R}_{g'g'}(\Delta z, c), \end{aligned} \tag{6}$$

where the correlations are not yet normalized. If the perturbation g' and the true signal g are independent of each other the correlation $\hat{R}_{gg'}$ will be zero, and this is assumed. The last term, $\hat{R}_{g'g'}$, will be taken as the auto-correlation of a random image with concentration c and artificial particle width w. This correlation can be computed by placing particles at random positions, thus producing an artificial signal where the parameters c and w have been chosen to match the ones used for the experimental images.

When $\hat{R}_{gg'}$ is set to zero, and c and w are known, a perturbation-corrected correlation is obtained from equation 6 as:

$$R_{gg} = \frac{\hat{R}_{ff} - \hat{R}_{g'g'}}{max(\hat{R}_{ff} - \hat{R}_{g'g'})}, \tag{7}$$

where the last step is to normalize the correlation.

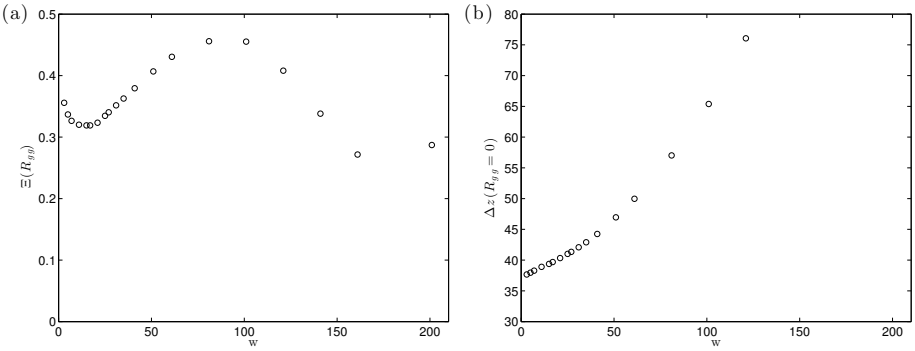

FIGURE 11. Streakiness (a) and streak widths (b) for different artificial particle width, w. The concentration 0.1 particles per column is used

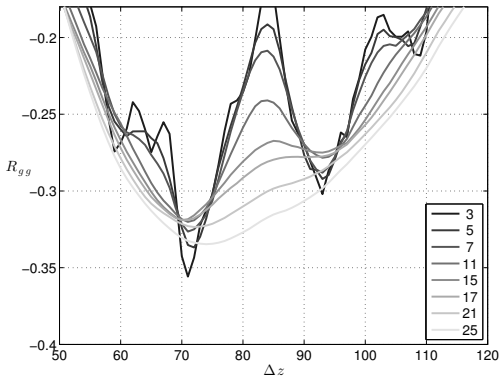

FIGURE 12. Close up off the correlation minima for different w for the same case as in Fig. 11

The streakiness and the streak width extracted from the true correlation R_{gg}, in turn calculated from equation 7 are shown in Figs. 10a and 10b, respectively. As before, ($\bullet, \blacksquare, \blacktriangleleft, \blacktriangleright, \blacktriangledown$) represents physically varied concentration and ($\circ, \square, \triangleleft, \triangleright, \triangledown$) represents artificially varied concentrations. In Fig. 10a, the apparent concentration dependency of the streakiness in cases 1-5 from Fig. 7a is cancelled for concentrations greater than $\sim$ 0.05 particles per column. Regarding the streak width, the concentration dependency is observed to be even better improved. For concentrations lower than 0.05 the assumption that g and g' are independent may not be true.

3.3b. *Artificial particle size w.* The solely free parameter is the artificial particle width. Fig. 11 depicts how (a) the streakiness and (b) the streak width

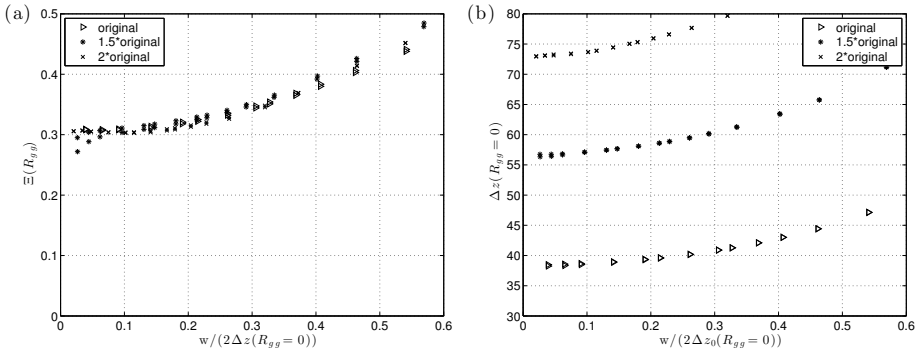

FIGURE 13. Streakiness (a) and streak widths (b) for different streak widths, a collapse of the curves is seen when plotted against $w/2\Delta z(R_{gg}=0)$ in (a). Original streak width, ($\triangleright$), all particle positions multiplied by 1.5, ($*$) and 2, ($\times$). The image size is kept constant and two concentrations are used (0.1 and 0.2 particles per column)

vary with the artificial particle width for case 1. It is clear that both of these sought quantities depend on w. The streak width increases with increasing w, while the streakiness on the other hand, first assumes a minimum and then a maximum as w increases. It should be noted that the maximum occurs at a particle width much larger compared to the streak width and is therefore disregarded.

In Fig. 12 a close up of the correlation minima for $w = 3, 5, 7, 11, 15, 17, 21, 25$ pixels are displayed, corresponding to the eight lowest w-values in Fig. 11a and 11b. As w increases the correlation is seen to become smoother, explaining the minimum in Fig. 11a. As low value as possible for w is wanted, but the correlation must be smooth enough to have a well defined minimum.

3.3c. *Streakiness dependence on streak width.* Since the positions of all particles are known it is easy to test the dependency of streakiness on streak width. When the streak width is artificially changed by multiplying all particle positions with a constant, the effect on the streakiness can be observed. Preferably the streakiness would be constant. Fig. 13 displays three different cases, first the original case ($\triangleright$), and also two cases where the positions of all particles have been multiplied by the factors 1.5 ($*$) and 2 ($\times$). The image size is kept constant. When w is normalized with the streak width, $2\Delta z(R_{gg} = 0)$, the curves collapse.

The image finite size finally also needs to be accounted for, due to the loss in information in the auto-correlation. The correlations in Fig. 13 are therefore normalized with $(1 - \Delta z/\text{image size})$, and so are all results from

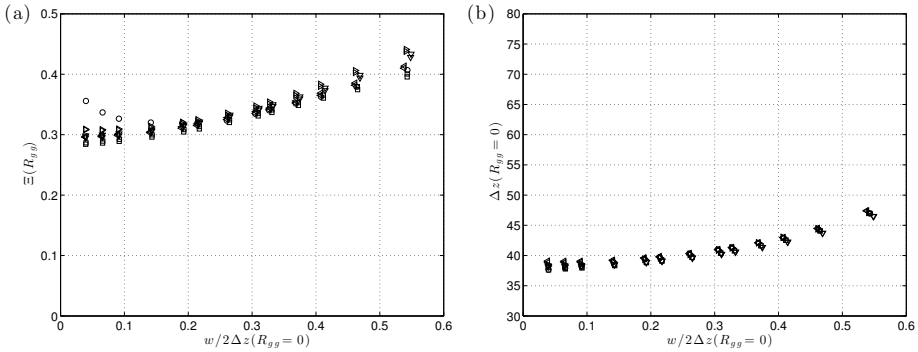

FIGURE 14. Streakiness (a) and streak widths (b) for different artificial particle width, w. Cases 1-5 with two concentrations, 0.1 and 0.2 particles per column, each are displayed $(\circ, \square, \triangleleft, \triangleright, \triangledown)$

here on. This step makes the method independent of image size, Isermann & Münchhof (2011).

The information from this section shows that it is possible to compare the streakiness qualitatively between two different experiments if the same value of $w/2\Delta z(R_{gg} = 0)$ is used, and the image size is taken into account through the normalization above.

3.3d. *Streakiness at* $w/2\Delta z(R_{gg} = 0) = 0.2$, $\Xi(R_{gg})_{0.2}$. The final streakiness values, $\Xi(R_{gg})$, and streak widths, $\Delta z(R_{gg} = 0)$ are plotted against the artificial particle width normalized by the streak width in Fig. 14. The concentrations shown are 0.1 and 0.2 particles per column for the five cases, $(\circ, \square, \triangleleft, \triangleright, \triangledown)$, except for the lowest concentration case that has a physical concentration of only 0.12 particles per column. The spread of $\Xi(R_{gg})$, due to jagged correlations at small $w/2\Delta z(R_{gg} = 0)$, for the lowest concentration $(\circ)$, is the reason for the streakiness to be taken as the value at $w/2\Delta z(R_{gg} = 0) = 0.2$. A subscript is introduced to the streakiness notation, $\Xi(R_{gg})_{0.2}$, in order to indicate which relative particle width that is used. At $\Xi(R_{gg})_{0.2}$ both streakiness and streak width starts to increase, but the deviations up to this point are small.

4. Conclusions

A method that provides consistent measures of streakiness and streak width in particle images from different flow situations has been developed and verified. The final method is independent of particle concentration, image size and streak width as well as the parameters of the method itself.

First, two particle streak analysis methods have been compared and evaluated. The two methods were based on particle positions, summation of images

and a following correlation. The streak width and the streakiness were sought. The streak half width, Δz, was taken as the first zero-crossing of the correlation and the streakiness, $\Xi(R_{II}) = |min(R_{II})|$. The first method was based on Voronoi analysis and the second on artificial particles with an assigned fixed width. Both methods were shown to possess a severe concentration dependence.

However, the streak width was shown to be constant at concentrations greater than ~ 0.1 particles per column for the fixed width method. The fixed width method was improved and an expression was derived to account for the concentration dependence of the streakiness. The derivation was based on a random image significantly contribute to the total correlation at low concentrations. After this correction, the streakiness was shown to be independent of concentrations lower than ~ 0.05 particles per column. Furthermore, scaling the artificial particle width with the streak width made the streakiness independent of streak width. Therefore, and because of the need to smoothen the correlation, it is proposed to set the artificial particle width to 20% of the streak width, denoted $\Xi(R_{gg})_{0.2}$.

Acknowledgements

Mr Joseph Fjellgren is acknowledged for the schematic drawing of the setup. This work was funded by the Knut and Alice Wallenberg Foundation, through the Wallenberg Wood Science Center. Dr. Lundell and Dr. Prahl Wittberg has also been funded by the Swedish Research Council.

References

Carlsson, A., Håkansson, K., Kvick, M., Lundell, F. & Söderberg, L. D. 2011 Evaluation of steerable filter for detection of fibers in flowing suspensions. *Exp in Fluids* **51**, 987–996.

Fessler, J. R., Kulick, J. D. & Eaton, J. K. 1994 Preferential concentration of heavy particles in a turbulent channel flow. *Phys Fluids* **6** (11), 3742–3749.

Fransson, J. H. M. & Alfredsson, P. H. 2003 On the disturbance growth in an asymptotic suction boundary layer. *J Fluid Mech* **482**, 51–90.

Isermann, R. & Münchhof, M. 2011 Correlation analysis with discrete time models. In *Identification of Dynamic Systems*, pp. 179–200. Springer Berlin Heidelberg.

Kaftori, D., Hetsroni, G. & Banerjee, S. 1995*a* Particle behavior in the turbulent boundary layer. I. Motion, deposition, and entrainment. *Phys Fluids* **7** (5), 1095–1106.

Kaftori, D., Hetsroni, G. & Banerjee, S. 1995*b* Particle behavior in the turbulent boundary layer. II. Velocity and distribution profiles. *Phys Fluids* **7** (5), 1107–1121.

Kulick, J. D., Fessler, J. R. & Eaton, J. K. 1994 Particle response and turbulence modification in fully developed channel flow. *J Fluid Mech* **277**, 109–134.

Kvick, M., Håkansson, K., Lundell, F., Prahl Wittberg, L. & Söderberg, L. D. 2012 Fibre orientation and fibre streaks in turbulent half channel flow. To be submitted .

Lagraa, B., Labraga, L. & Mazouz, A. 2004 Characterization of low-speed streaks in the near-wall region of a turbulent boundary layer. *European J Mech - B/Fluids* **23** (4), 587 – 599.

Marchioli, C., Fantoni, M. & Soldati, A. 2010 Orientation, distribution, and deposition of elongated, inertial fibers in turbulent channel flow. *Phys Fluids* **22** (3), 033301.

Monchaux, R., Bourgoin, M. & Cartellier, A. 2010 Preferential concentration of heavy particles: A voronoï analysis. *Phys Fluids* **22** (10), 103304.

Narayanan, C., Lakehal, D., Botto, L. & Soldati, A. 2003 Mechanisms of particle deposition in a fully developed turbulent open channel flow. *Phys Fluids* **15** (3), 763–775.

Ninto, Y. & Garcia, M. H. 1996 Experiments on particle wall region of an open channel flow: implications for sediment transport. *J Fluid Mech* **326**, 285–319.

Pedinotti, S., Mariotti, G. & Banerjee, S. 1992 Direct numerical simulation of particle behaviour in the wall region of turbulent flows in horizontal channels. *Int J Multiph Flow* **18** (6), 927–941.

Rashidi, M., Hetsroni, G. & Banerjee, S. 1990 Particle-turbulence interaction in a boundary layer. *Int J Multiph Flow* **16** (6), 935–949.

Rouson, D. W. I. & Eaton, J. K. 2001 On the preferential concentration of solid particles in turbulent channel flow. *J Fluid Mech* **428**, 149–169.

2

Paper 2

Fibre orientation and fibre streaks in turbulent wall bounded flow

By Mathias Kvick, Karl Håkansson, Fredrik Lundell, Lisa Prahl Wittberg & L. Daniel Söderberg

Wallenberg Wood Science Center & Linné Flow Centre, KTH Mechanics, Royal Institute of Technology, SE – 100 44 Stockholm, Sweden

To be submitted

The behaviour of fibres in a wall bounded turbulent shear flow is investigated. Understanding and modelling of fiber suspension flow is necessary for improvements in many applications, e.g. papermaking. Experimental data covering wide parameter spaces is an important ingredient in this effort. A dilute fibre suspension flowing down an inclined glass plate is studied. Images of the fibres in the flow are acquired from beneath the glass plate and the images are analysed using a steerable filter, providing the position and orientation of the fibres. Both fibre orientation distributions and spatial distributions are investigated. It is found that the length of the fibres plays an important role in the overall fibre orientation distribution. The flow conditions are also observed to have an effect on the orientation on the shorter fibres. A small amount of polymers added to the suspension is found to have an impact on the fibre orientation. Furthermore, the results indicate that increased fibre concentration drives the fibres towards a particular orientation, indicating that fibre interactions cannot be modelled as a solemny diffusive effect in this case. Moreover, the fibres are found to form streamwise streaks of different intensity. The width of these streaks are measured and corresponds to the same width as the low velocity streaks found in turbulent wall layers. The intensity of the fibre streaks are found to vary with the flow conditions.

1. Introduction

When producing paper, the mass and orientation distribution of cellulose fibres, and therefore also the mechanical properties of the paper are highly dependent on the flow in the headbox nozzle, Cox (1952), Lundell *et al.* (2011). The headbox is a 2D contraction generating a thin, wide fibre suspension sheet that is jetted out onto permeable forming wires, where the paper is formed. The flow in the headbox is highly complex, being both turbulent and extensional as well as having walls and vanes present. Increasing the knowledge of the behaviour

of fibres in turbulent wall bounded flows will provide better understanding of the effects the headbox has on the final paper. Not only the distribution of the fibre orientations, i.e. their individual direction in the flow, but also the overall fibre orientation and the distribution of the fibres in the cross direction (spanwise) is of interest.

Carlsson *et al.* (2007) and Carlsson (2009) studied a laminar half channel flow with a dilute fibre suspension. The focus was mainly on fibre orientation and fibre location in the wall normal direction. The fibres had a density greater than that of the liquid phase. It was concluded that most fibres with small aspect ratio were located closer than half of a fibre length from the wall and aligned perpendicular to the flow. On the other hand, fibres with greater aspect ratios were found to be located at distances more than half a fibre length away from the wall and oriented in the flow direction. It was suggested that this behaviour occured due to a competition between fluid inertia (driving the fibres towards the flow direction) and the combination of sedimentation and wall contacts (driving the fibres away from the flow direction).

Particle streaks have been observed both in experiments and simulations of spherical particles in turbulent channel flow (e.g. Kaftori *et al.* (1995*a*), Kaftori *et al.* (1995*b*), Ninto & Garcia (1996), Marchioli & Soldati (2002) and Narayanan *et al.* (2003)). Marchioli & Soldati (2002) concluded that the largest preferential concentration occurs close to the wall, and the particles accumulate in the low speed velocity streaks.

Zhang *et al.* (2001), Mortensen *et al.* (2008) and Marchioli *et al.* (2010) performed DNS (Direct Numerical Simulation) of fibre suspensions in turbulent channel flow. Zhang *et al.* (2001) studied the transport and deposition of fibres while Mortensen *et al.* (2008) as well as Marchioli *et al.* (2010) investigated the effects of aspect ratio and response time on the orientation of the fibres. In all the above mentioned studies the non-spherical particles also accumulated in the low velocity streaks and the fibres tended to align in the flow direction with increasing aspect ratio.

In this study, the orientation and accumulation of fibres in turbulent half channel flow is investigated experimentally. Quantified data is obtained and discussed. The results provide several distinct observations that can be used for development and verification of numerical models. In section 2 the experimental setup and the methods used to extract data is explained. The results are presented in sections 3 and 4, focussing on fibre orientation as well as the effect of polymers and investigating streamwise streaks of high local fibre concentration. In section 5 the results are discussed and the conclusions are summarised in section 6.

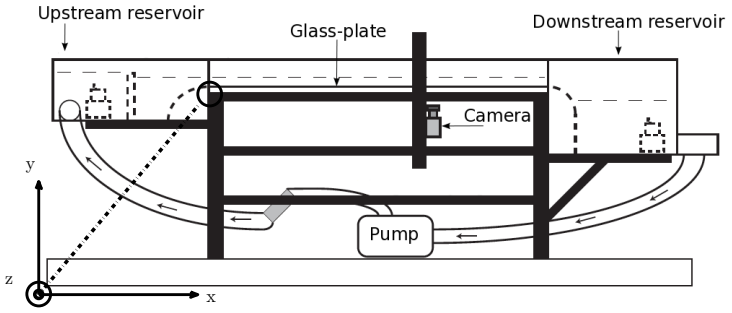

FIGURE 1. Schematic of the water-table, camera and pumps. The length of the glass plate is approximately 2 m and the width 0.6 m.

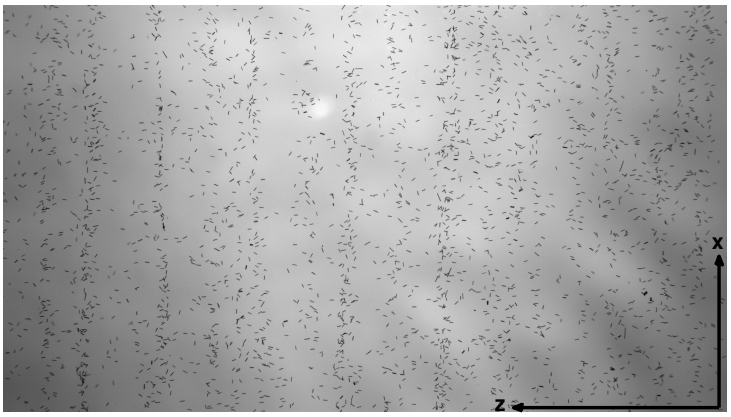

FIGURE 2. Typical image of the fibre suspension acquired during experiment. The flow is in positive x-direction. The black dyed fibres can clearly be seen in the flow. The dimensions of the image is $\Delta x = 5$ cm and $\Delta z = 10$ cm.

2. Methods

2.1. *Flow apparatus and image acquisition*

The experimental setup consisted of a water-table and a camera, shown in figure 1. The water-table was filled with a dilute suspension of fibres and water. The suspension was pumped from a downstream reservoir to an upstream reservoir and was free to flow down an inclined glass plate to the downstream reservoir. Submersible pumps were placed in the upstream and downstream reservoirs stirring the suspension and preventing fibres from sedimenting there.

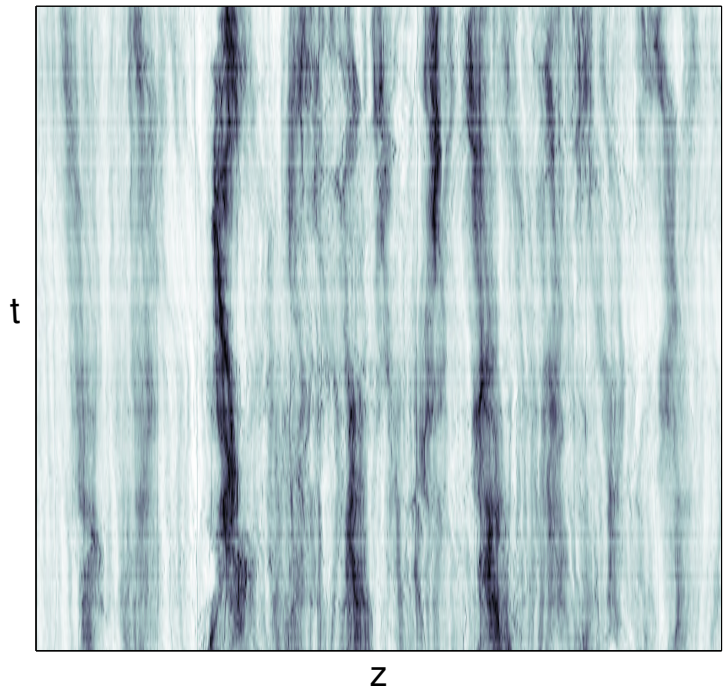

FIGURE 3. Visualisation of fibre streaks in time, where each row corresponds to an image such as figure 2 summed in the streamwise direction, $\Delta z = 10$ cm and total time lapse $\Delta t = 7.7$ s.

Underneath the glass plate, at a downstream position, a camera was placed in order to acquire images of the fibres in the flowing suspension. A stroboscope was mounted close to the camera and produced short flashes in order to generate sharp images. The depth of field of the camera lens was enough to detect all fibres in the water layer in all experiments regardless of the fibres wall normal position. However, at the acquisition position, located 1100 mm downstream of the inlet of the glass plate, most fibres were observed to have sedimented and be located in the direct proximity of the wall. A typical image of the suspension is shown in figure 2, corresponding to the x-z plane, where x, y, z are the flow, wall normal and spanwise directions, respectively. The origin is positioned on the leading edge of the glass plate with $z = 0$ on its centreline. In each experiment, 150 images were acquired and in each image $200 - 3000$ fibres were detected, ensuring converging statistics. In most experiments, fibres could be seen to gather in streamwise streaks, a visualisation of these fibre streaks is displayed in figure 3. This figure is based on 96 images captured during 7.7 s;

each image is summed in the streamwise direction and is a row in the final figure.

The flow down the glass plate was driven by gravity alone, and thus the wall shear stress, τ_w, can be calculated through a force balance between the glass plate and the water layer (e.g. Acheson (1995));

$$\tau_w = \rho g h \sin\alpha. \tag{1}$$

Here ρ is the density of water, g is the gravitational acceleration, h is the height of the water layer and α is the inclination angle of the glass plate. The flow can be seen as an approximation of a half-channel flow, since the velocity gradient is zero on the centreline of a full channel (with height $2h$). Due to the large viscosity difference between water and air the conditions on the free surface in the present setup are very close to this condition.

In a channel flow, the friction Reynolds number is defined as:

$$Re_\tau = \frac{h}{\nu} u_\tau = \frac{h}{\nu}\sqrt{\frac{\tau_w}{\rho}} = \frac{h\sqrt{gh\sin\alpha}}{\nu}, \tag{2}$$

where $u_\tau = \sqrt{\tau_w/\rho}$ is the friction velocity and ν is the kinematic viscosity. Note that Re_τ is only dependent on material properties and the geometry of the channel. The effects of fluid and particle inertia on particle rotation (for a given density ratio) is quantified by a particle Reynolds number Re_p defined as (Aidun *et al.* 1998):

$$Re_p = \dot{\gamma}\frac{l_f^2}{\nu} = \frac{\tau_w}{\rho\nu}\frac{l_f^2}{\nu} = \frac{l_f^2 g h \sin\alpha}{\nu^2}, \tag{3}$$

where $\dot{\gamma}$ represents the shear rate at the glass plate and l_f is the fibre length. Ad defined here, Re_p characterises the hydrodynamic torques acting on the particles in the flow. The actual water layer thickness, h, is 8—12 mm depending on parameter combination.

Rigid cellulose acetate fibres with a density of $\rho_f = 1300$ kg/m^3 and aspect ratios $r_p = 7, 14$ and 28, corresponding to fibre lengths $l_f = 0.5, 1$ and 2 mm and cross section 70 μm, were mixed with 120 l of water, resulting in low concentration suspensions ($0.00042 - 0.0033\%$ by weight, corresponding to a number density of $nl^3 = 0.0008 - 0.0066$). However, due to sedimentation, most fibres were located close to the wall, resulting in higher local concentration. The local concentration was calculated via the number of fibres in each image. For one flow case, the effect of concentration was studied using concentrations up to $nl^3 = 0.031$. Only mono dispersed suspensions were studied.

The setup was limited to $\mathrm{Re}_\tau \leq 210$, due to the generation of surface waves at higher Reynolds numbers.

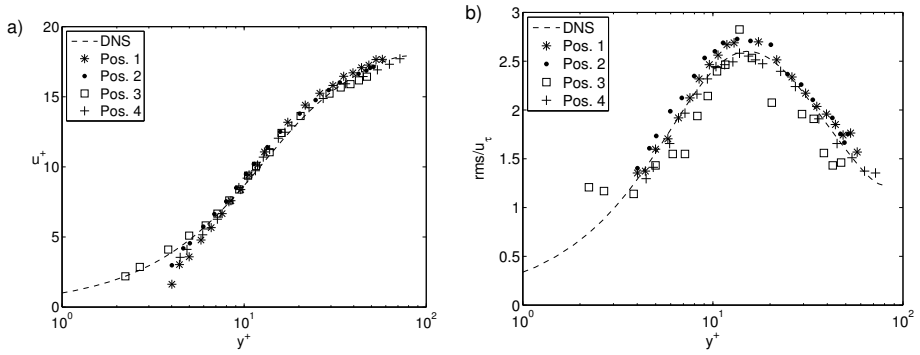

FIGURE 4. Velocity statistics measured by LDV at $(x, z) = (1100, 0)$ mm, $(1100, \pm 200)$ mm and $(800, 0)$ mm, positions 1, 2, 3 and 4, respectively, at $\mathrm{Re}_\tau = 88$. The experimental data is compared to DNS-data from a full channel flow at $\mathrm{Re}_\tau = 80$. (a) Mean velocity profiles. (b) Velocity fluctuations.

2.2. *Laser doppler velocimetry*

In order to ensure that the flow is fully developed and homogenous, Laser Doppler Velocimetry (LDV) measurements without fibres were carried out at $(x, z) = (1100, 0)$ mm, $(1100, \pm 200)$ mm and $(800, 0)$ mm. Streamwise velocity and *rms* profiles for $\mathrm{Re}_\tau = 88$ are displayed in figure 4, where the dashed lines are comparisons with DNS for a full channel flow at $\mathrm{Re}_\tau = 80$ (Tsukahara *et al.* 2005). The agreement between the experiment and DNS is good. The velocities are normalized with u_τ and the vertical coordinate with the viscous length scale $l^+ = \nu/u_\tau$.

2.3. *Fibre detection and streak analysis*

The images were processed by first subtracting the background noise. The fibres position (x- and z-coordinate in the image), and the orientation angle β (measured as positive rotation around the y-axis where $\beta = 0$ is the flow direction) were obtained using a second order ridge detector within the class of steerable filters, Jacob & Unser (2004). The filter has earlier been evaluated by Carlsson *et al.* (2011), reporting the effect of noise and unsharpness of the images on the orientation angle to be less than 1° for moderate levels of disturbances.

In order to analyse the accumulation of fibres into streamwise streaks, observed in the experiments, the method described in Håkansson *et al.* (2012) was applied. In short, the fibre positions are used to create an image with artificial fibres where the orientation and size of the fibres are identical. The new image is summed in the streamwise direction. The resulting signal is

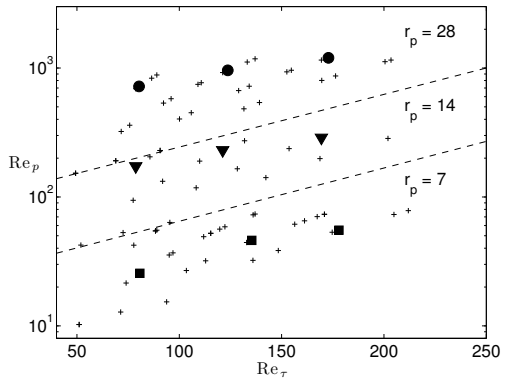

FIGURE 5. Parameter combinations studied, (+) indicate all measurements made. Measurements marked with the symbols (●, ▼, ■) corresponds to the data shown in figure 6. At each marked position, 150 images have been acquired and analysed. Three distinct regions are shown in which the aspect ratio is constant.

correlated with itself, which, when performed for a whole set of images, results in a mean streak width and a mean streakiness of the fibre structure. In the analysis, great care is taken to compensate for the influence of concentration, image size, fibre size and streak width.

3. Fibre orientation results

In figure 5, the parameter combinations at which measurements have been performed are shown. The friction Reynolds number, Re_τ, was varied between 50 and 210, and the particle Reynolds number, Re_p between 10 and 10^3. Note that the parameter space can be divided into three regions, without overlap, where each region corresponds to one of the three aspect ratios.

In the following sections the effect of aspect ratio, Re_τ, downstream position and concentration on the fibre orientation will be investigated. The effect on fibre orientation of small amount of polymers in the suspension is also studied. Fibre orientation and anisotropy data will be presented.

3.1. *Anisotropy*

In order to quantify the anisotropy of the fibre orientation distribution, a unit vector $\mathbf{p}$ is associated with each fibre, Advani & Tucker III (1987). The components of $\mathbf{p}$ are directly related to the orientation of the fibre. In this case, since the acquired orientation is 2 - dimensional, only one orientation angle, β,

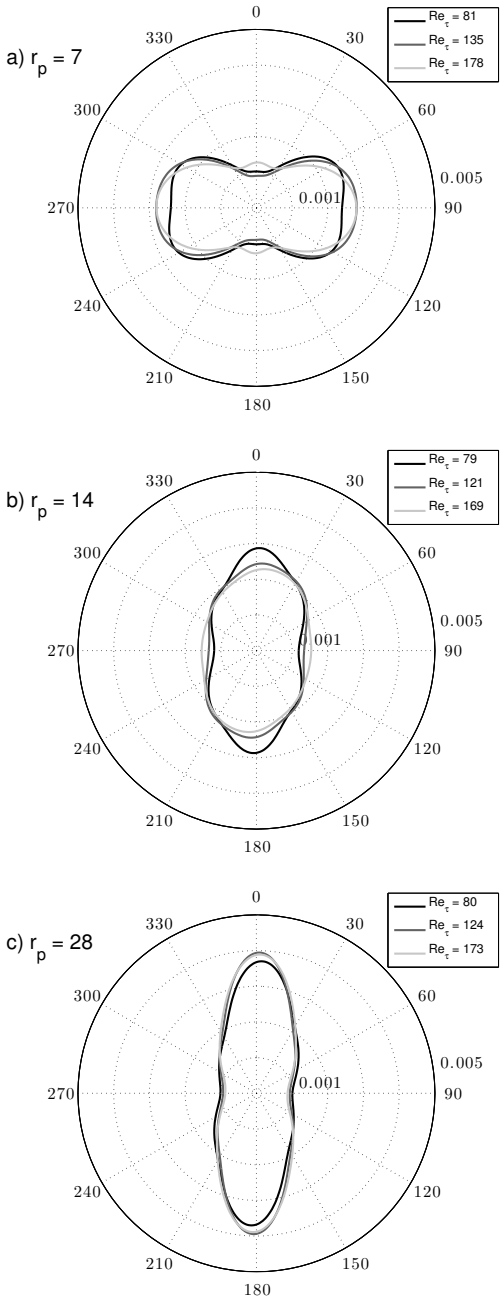

FIGURE 6. Fibre orientation distributions for (a) $r_p = 7$, (b) $r_p = 14$ and (c) $r_p = 28$, at positions in the parameter space marked with (●, ▼, ■) in figure 5.

is used.

$$p_1 = \int_0^\pi \cos\beta \ \mathrm{d}\beta$$
$$p_2 = \int_0^\pi \sin\beta \ \mathrm{d}\beta \tag{4}$$

The components of the second order orientation tensor $\mathbf{a}_2$ in which $a_{ij} = p_i p_j$ are now defined as;

$$a_{11} = \int_0^\pi \cos^2\beta \ \mathrm{d}\beta$$
$$a_{12} = a_{21} = \int_0^\pi \cos\beta sin\beta \ \mathrm{d}\beta \tag{5}$$
$$a_{22} = \int_0^\pi \sin^2\beta \ \mathrm{d}\beta$$

The anisotropy is then obtained as follows;

$$A = a_{11}/a_{22}.$$

3.2. *Orientation distributions and effect of aspect ratio*

In figures 6a–6c, fibre orientation distributions for the different aspect ratios at similar friction Reynolds numbers are displayed. The orientation angle, β, is defined to be zero, ($\beta = 0$), in the streamwise direction, and $\beta = 90$ in the spanwise direction. It is evident from the figures that the aspect ratio plays an important role for the fibre orientation distribution. In figure 6a, showing the fibre orientation distribution for the shortest fibres (aspect ratio $r_p = 7$), most of the fibres are located between 45 and 135 degrees, as well as between 225 and 315 degrees since the distribution is symmetric. A large difference is found if comparing with figure 6c, in which the fibre orientation distribution for fibres with aspect ratio $r_p = 28$ is shown, where most fibres have an orientation close to $\beta = 0°$, *i.e.* the streamwise direction.

As shown in figure 7, the fibres with aspect ratios $r_p = 28, (\bullet)$ and $r_p = 7, (\blacksquare)$, are oriented ($A = 2$ and 0.5, respectively), while the medium length fibres, $r_p = 14, (\blacktriangledown)$ are more isotropic. This information is also possible to visually extract from the fibre orientation distributions in figure 6.

3.2a. *Effect of Re_τ.* In figure 7, the anisotropy for all measurements are shown versus the friction Reynolds number. For the longer fibres, with aspect ratio $r_p = 28, (\bullet)$, A shows no distinct trend. For fibres with $r_p = 14, (\blacktriangledown)$, A decreases with a near constant slope. For the shortest fibres, $r_p = 7, (\blacksquare)$, A first decreases, assumes a minimum at $\mathrm{Re}_\tau \approx 110$, and thereafter increases with increasing Re_τ. For the two shorter fibres, the anisotropy A approaches 1, as Re_τ increases, indicating an approach to isotropy. The open symbols in figure 7 refer to concentration variations and will be discussed later.

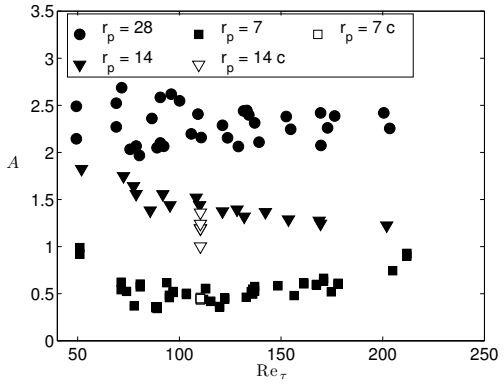

FIGURE 7. Anisotropy for all measurements versus Re_τ, where $(\bullet, \blacktriangledown, \blacksquare)$ represents $r_p = 28$, $r_p = 14$ and $r_p = 7$, respectively and $\triangledown, \square$ represents measurements where only the concentration of fibres have been altered, the exact concentrations can be found in figure 9c.

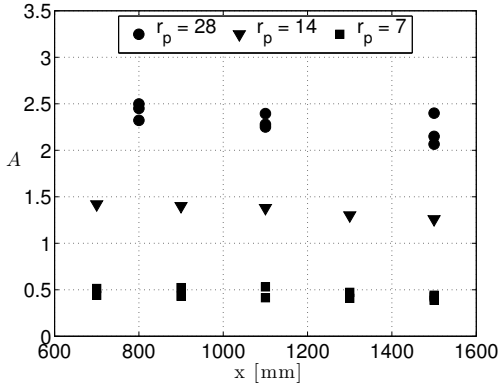

FIGURE 8. Anisotropy as a function of streamwise position; $(\bullet)$ for $r_p = 28$, $(\blacktriangledown)$ for $r_p = 14$ and $(\blacksquare)$ for $r_p = 7$, where the downstream position has been changed for each aspect ratio. $\mathrm{Re}_\tau = 100 - 200$ and $\mathrm{Re}_p = 200 - 1100$. The acquisition point used for all other measurements are located at 1100 mm downstream from the beginning of the glass plate.

3.2b. *Effect of downstream position.* The anisotropy at several streamwise positions is plotted in figure 8. The measurements have been performed with different fibre lengths as well as for different friction Reynolds numbers, ranging from 100 to 200. All fibre lengths have a slight decrease in anisotropy as

the fibres progress downstream, indicating that the fibre orientation distributions are not fully developed at the acquisition point. However, the change in anisotropy is slow, implying that the major changes in orientation has occurred further upstream.

3.2c. *Effect of number of fibres.* Since the local concentration reached in the experiments is believed to fall into the semi-dilute regime, experiments were performed for constant flow conditions and varied concentrations. In figure 9, results of fibre orientation from experiments with different fibre concentration is displayed; (a) and (b) as well as the open symbols in (c) show data from $\mathrm{Re}_\tau = 110$ and constant Re_p for each aspect ratio whereas the filled symbols are all the cases shown in figure 5. The concentration variations from $\mathrm{Re}_\tau = 110$ are also shown with open symbols in figure 7.

Here the local concentration is computed from the mean number of fibres found in each set of images. Figure 9a and 9b shows the orientation distributions for fibres with $r_p = 7$ and $r_p = 14$ respectively, and in figure 9c, the anisotropy is plotted. The squares (open and closed) in figure 9c implies that the local concentration has no impact on the shorter fibres, whereas for the intermediate fibres ($\blacktriangledown, \triangledown$) A increases from close to unity with increasing concentration. The post processing fibre detection algorithm was limiting the experiment in terms of studying greater concentrations. The orientation distributions are not longer constant at $nl^3 > 0.01$, indicating that the suspension no longer is dilute.

3.2d. *Effect of polymers.* The addition of polymers to the suspension is interesting from an orientation control point of view. Therefore experiments with a small addition (40ppm) of Poly-Ethylene-Oxide (PEO) were performed. Viscosity measurements of the fluid phase with a rotational viscometer were performed in order to ensure that the shear viscosity was not changed as compared to water. Fibres with aspect ratios 7 and 14 where used at different friction Reynolds numbers, the results are shown in figure 10. The anisotropy is not notably changed for $r_p = 7$. However, for $r_p = 14$, all measurements have a lower anisotropy compared to the case where the fluid phase is water. Polymers have in previous studies, White *et al.* (2004), been shown to interact with and to modify the quasi streamwise streaks in a turbulent wall bounded flow. Furthermore, White *et al.* (2004) found that the addition of polymers had an effect on the buffer layer, which could be the reason for the results displayed in figure 10. Since the length of the fibres with aspect ratio 14 ($l_f = 6l^+ - 18l^+$) corresponds to the location of the buffer layer, while the shorter fibres with aspect ratio 7 have a length ($l_f = 3l^+ - 9l^+$) that is close to the height of the viscous sublayer.

3.2e. *Orientation in streaks.* In order to investigate whether fibres inside streaks are oriented differently as compared to fibres not located in streaks, the 10%

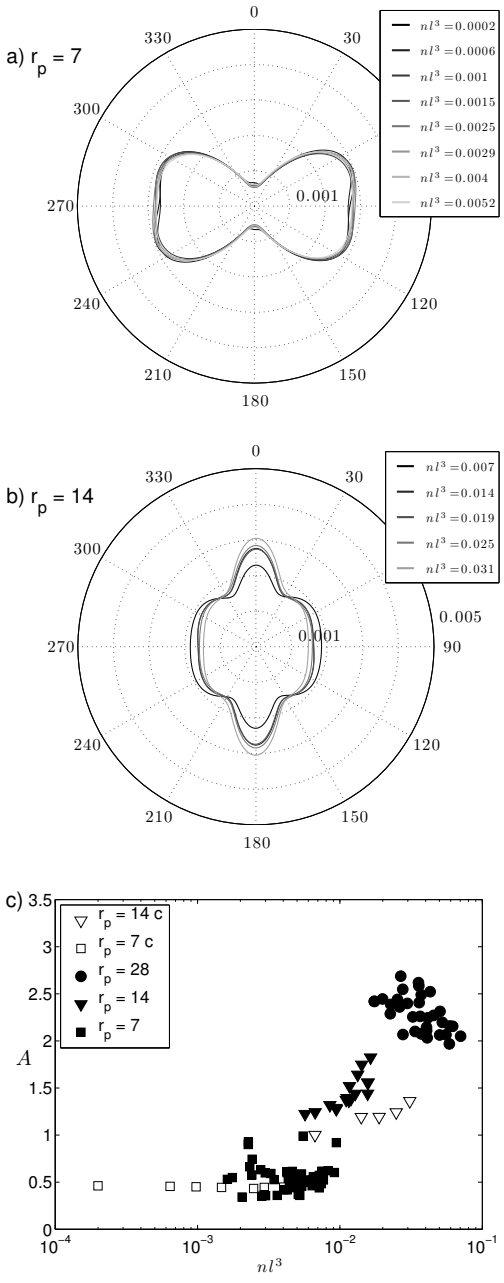

FIGURE 9. Orientation distributions of fibres with (a) $r_p = 7$ and (b) $r_p = 14$, where the concentration has been changed for each aspect ratio. $\mathrm{Re}_\tau = 110$. c) Anisotropy quotient versus nl^3, where open symbols (□ and ▽) represents the measurements in (a) and (b) where the flow conditions have been kept constant, the filled symbols (●, ▼, ■) represents all measurements performed, including different Re_τ.

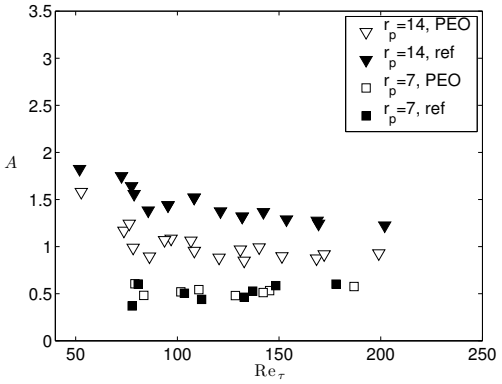

FIGURE 10. Anisotropy for suspension containing PEO (▽ and □) compared to the reference (▼ and ■) where the fluid phase is tap water.

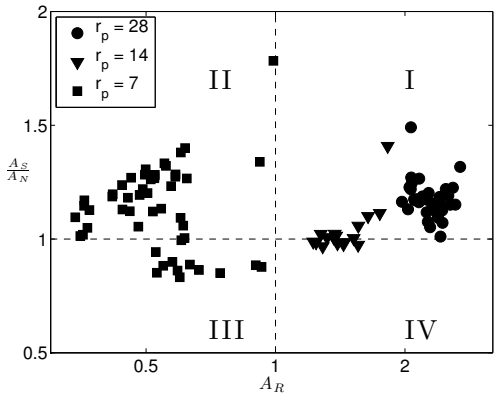

FIGURE 11. Quota of the anisotropy for fibres inside, A_S, and outside, A_N, of streaks compared with the reference anisotropy, A_R, for all cases.

most clustered (from Voronoi analysis) fibres in each image are defined to be in streaks, and the 10% least clustered are considered to be located outside the streaks. Figure 11 shows the anisotropy in streaks, A_S, normalised with anisotropy of the fibres that are not in streaks, A_N, as function of the original (reference) anisotropy of all fibres in the measurement. The results in this plot belong to one of four quadrants I-IV. Data points in quadrants I and III means that the fibres in the streaks have a preferred orientation (in the flow direction in I and normal to the flow in III) compared to the fibres outside streaks. Data points in quadrants II and IV, on the other hand, means that the fibres in the

streaks have a more random orientation than the fibres outside of the streaks. The main observation from figure 11 is that for the cases with high A_R the fibres in the streaks tend to be even more aligned than the fibres outside the streaks. (compare quadrant I and IV).

4. Streakiness and fibre streak width results

In most experiments, the fibres accumulated in long streamwise streaks.

In figure 12a, the relative streakiness, Ξ, is shown as a function of Re_τ. The larger the dot, the stronger the tendency for the fibres to accumulate into streamwise streaks. The measurements marked with a ($\times$) could not be evaluated due to too low (streakiness analysis) or too high (fibre detection) fibre concentration. Moreover, the streakiness displays a maximum at $\mathrm{Re}_\tau \approx 110$ as is shown in figure 12b, where the relative streakiness is depicted as function of Re_τ.

In figure 12c the width of the fibre streaks are compared with the value $50l^+$ (full line), an empirical value of the streak width of the low velocity streaks, e.g. Zacksenhouse *et al.* (2001). The dashed line represents $70l^+$ and figure 12c shows that most experimental streak widths fall in between these two line. The fibre streaks scale in the same manner as low velocity streaks in a flow without fibres, although slightly wider. Similar behaviour has been reported for spherical particles in channel flows where the spheres has been observed to widen the velocity streaks, Zhao *et al.* (2010).

5. Discussion

The results show a major impact of fibre aspect ratio on the orientation of the fibres as they have sedimented to the wall region. In comparison with the major impact of fibre aspect ratio, effects such as Reynolds number, concentration and addition of 40 ppm PEO are of secondary importance. These factors only modify the fibre orientation slightly. The orientation behaviour is such that shorter fibres ($r_p = 7$) are oriented normal to the flow direction whereas long fibres ($r_p = 28$) are oriented in the flow direction. The intermediate fibres ($r_p = 14$) give more isotropic orientation distributions.

This orientational behaviour is similar to the one observed in experiments on fibre orientation in laminar flow by Carlsson *et al.* (2007), Carlsson (2009). In the laminar case, a combined theoretical/numerical study showed that the difference in orientational behaviour between short and long fibres occurred due to a competition between the effects of sedimentation towards the wall and direct wall interaction (driving the fibres towards an orientation normal to the flow) and the effects of fluid inertia (when leaving the Stokes flow limit) counteracting this tendency.

In the present work, the turbulent case studied also contain particle inertia, turbulent fluctuations as well as particle interaction. The fact that the laminar

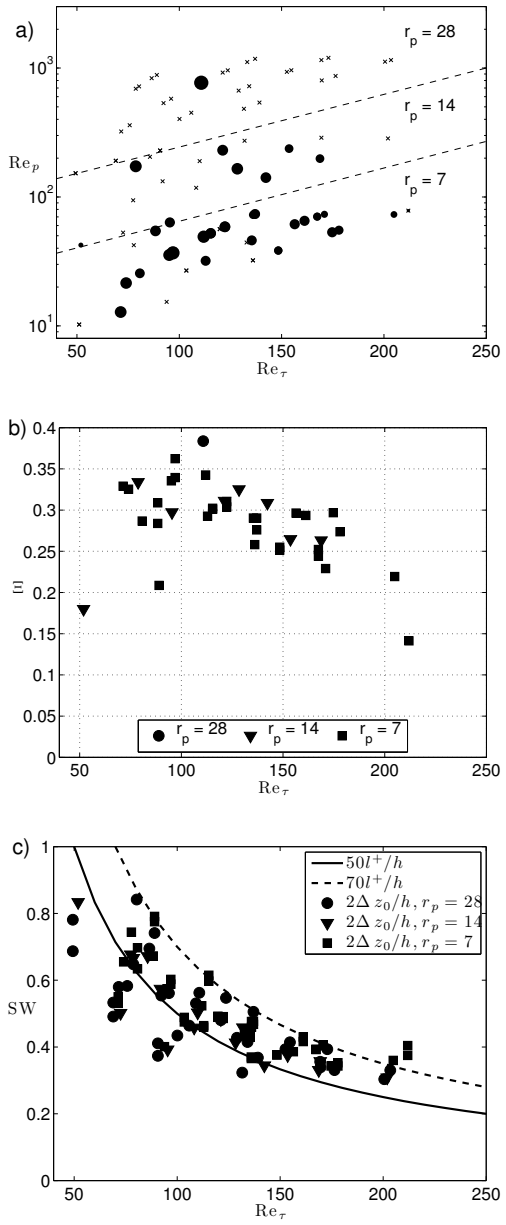

FIGURE 12. (a) Streakiness, bigger dots represent a higher degree of streakiness; (×) represents measurements were streakiness data could not be determined due to insufficient or excessive fibre concentration. (b) Relative streakiness, Ξ, as function of Re_τ, higher value represents higher streakiness. (c) streak widths normalised with the height of the waterlayer for $r_p = 28$ (•), $r_p = 14$ (▼) , $r_p = 7$ (■), 50 l^+/h (full line) and 70 l^+/h (dashed line).

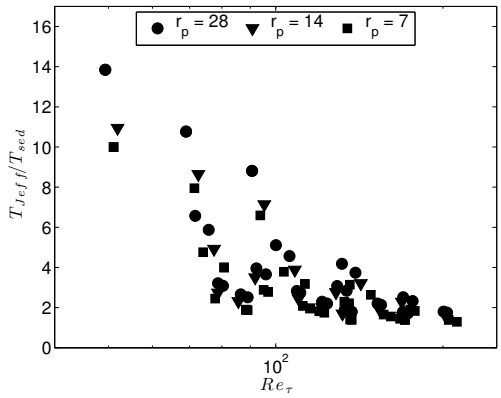

FIGURE 13. The ratio of the Jeffrey period and the sedimentation time from half a fibre length versus the friction Reynolds number.

and turbulent case are fairly similar shows that a detailed modelling of the physics of the hydrodynamic and direct interaction with the wall together with particle and fluid inertia are important. Once such models are at hand, the effect of different components of this complex system can be evaluated. It is possible that the similarity between the laminar and the turbulent results are a coincidence and that the present observations are a results of fibre interaction with the turbulence.

Thus, even though the number of Jeffery periods, Jeffery (1922), performed by the fibres during the time at which they interact directly with the wall is fairly low (see figure 13), the interactions with the wall are probably critical.

Two final points will be made that are both related to the concept of diffusivity. The present results indicate that the orientation of the fibres is governed by mean shear and wall interactions, even though the turbulence have a clear impact on organising the fibres into streaks. It should also be noted that the only distinct effect of concentration was an *increase* in anisotropy with increasing concentration, showing that the fibre interaction cannot be modelled as diffuse effects on the orientation distribution. Instead, the results indicate that increased fibre concentration drives the fibres towards a particular orientation (in our case an alignment in the flow direction).

6. Conclusions

Orientation and distribution of fibres in turbulent flow in the neighbourhood of a solid wall has been studied. The flow regime studied is $50 < \mathrm{Re}_\tau < 210$. The main conclusions are

- The fibre orientation depends on the fibre length normal to the flow for $r_p = 7$ and aligned with the flow for $r_p = 28$.
- The intermediate fibres ($r_p = 14$), displayed a more isotropic orientation distributions.
- For the intermediate fibres, the orientation distribution varied with concentration. At higher concentration, the fibre orientation was more anisotropic.
- A polymer (PEO) concentration of 40 ppm made the orientation distribution of the intermediate fibres more isotropic. The shorter fibres were not affected.
- The fibres organise themselves in streaks. The streakiness vary with Reynolds number and show a maximum around $\mathrm{Re}_\tau = 110$.
- The results indicate that fibre interactions cannot be modelled as a diffuse effect on the orientation.

Acknowledgements

Thanks to Dr. Allan Carlsson for providing valuable input during the experiment and analysis. Mr. Joseph Fjellgren is acknowledged for the schematic drawing of the setup. This work was funded by the Wallenberg Foundation, through the Wallenberg Wood Science Center. Dr. Lundell and Dr. Prahl Wittberg has also been funded by the Swedish Research Council.

References

Acheson, D. J. 1995 *Elementary Fluid Dynamics*. Oxford University Press.

Advani, S. G. & Tucker III, C. L. 1987 The use of tensors to describe and predict fiber orientation in short fiber composites. *Journal of Rheology* **31** (8), 751–784.

Aidun, C. K., Lu, Y. & Ding, E. 1998 Direct analysis of particulate suspensions with inertia using the discrete boltzmann equation. *Journal of Fluid Mechanics* **373**, 287–311.

Carlsson, A. 2009 Near wall fibre orientation in flowing suspensions. PhD thesis, KTH Mechanics, Royal Institute of Technology.

Carlsson, A., Håkansson, K., Kvick, M., Lundell, F. & Söderberg, L. D. 2011 Evaluation of steerable filter for detection of fibers in flowing suspensions. *Experiments in Fluids* **51**, 987–996.

Carlsson, A., Lundell, F. & Söderberg, L. D. 2007 Fiber orientation control related to papermaking. *Journal of Fluids Engineering* **129** (4), 457–465.

Cox, H. L. 1952 The elasticity and strength of paper and other fibrous materials. *British Journal of Applied Physics* **3** (3), 72.

Håkansson, K., Kvick, M., Lundell, F., Prahl-Wittberg, L. & Söderberg, L. D. 2012 Measurement of width and amplitude of particle streaks in turbulent flows. Manuscript in preparation.

Jacob, M. & Unser, M. 2004 Design of steerable filters for feature detection using canny-like criteria. *Pattern Analysis and Machine Intelligence, IEEE Transactions on* **26** (8), 1007 –1019.

Jeffery, G. B. 1922 The motion of ellipsoidal particles immersed in a viscous fluid. *Proceedings of the Royal Society of London. Series A, Containing Papers of a Mathematical and Physical Character* **102** (715), pp. 161–179.

Kaftori, D., Hetsroni, G. & Banerjee, S. 1995*a* Particle behavior in the turbulent boundary layer. I. motion, deposition, and entrainment. *Physics of Fluids* **7** (5), 1095–1106.

Kaftori, D., Hetsroni, G. & Banerjee, S. 1995*b* Particle behavior in the turbulent boundary layer. II. velocity and distribution profiles. *Physics of Fluids* **7** (5), 1107–1121.

Lundell, F., Söderberg, L. D. & Alfredsson, P. H. 2011 Fluid mechanics of papermaking. *Annual Review of Fluid Mechanics* **43** (1), 195–217.

Marchioli, C., Fantoni, M. & Soldati, A. 2010 Orientation, distribution, and deposition of elongated, inertial fibers in turbulent channel flow. *Physics of Fluids* **22** (3), 033301.

Marchioli, C. & Soldati, A. 2002 Mechanisms for particle transfer and segregation in a turbulent boundary layer. *Journal of Fluid Mechanics* **468**, 283–315.

Mortensen, P., Andersson, H., Gillissen, J. & Boersma, B. 2008 On the orientation of ellipsoidal particles in a turbulent shear flow. *International Journal of Multiphase Flow* **34** (7), 678 – 683.

Narayanan, C., Lakehal, D., Botto, L. & Soldati, A. 2003 Mechanisms of particle deposition in a fully developed turbulent open channel flow. *Physics of Fluids* **15** (3), 763–775.

Ninto, Y. & Garcia, M. H. 1996 Experiments on particlewall region of an open channel flow: implications for sediment transport. *Journal of Fluid Mechanics* **326**, 285–319.

Tsukahara, T., Seki, Y., Kawamura, H. & Tochio, D. 2005 DNS of turbulent channel flow at very low reynolds numbers. In *Proc. of the Fourth Int. Symp. on Turbulence and Shear Flow Phenomena*, pp. 935–940.

White, C., Somandepalli, V. & Mungal, M. 2004 The turbulence structure of drag-reduced boundary layer flow. *Experiments in Fluids* **36**, 62–69.

Zacksenhouse, M., Abramovich, G. & Hetsroni, G. 2001 Automatic spatial characterization of low-speed streaks from thermal images. *Experiments in Fluids* **31** (2), 229–239.

Zhang, H., Ahmadi, G., Fan, F.-G. & McLaughlin, J. B. 2001 Ellipsoidal particles transport and deposition in turbulent channel flows. *International Journal of Multiphase Flow* **27** (6), 971 – 1009.

Zhao, L. H., Andersson, H. I. & Gillissen, J. J. J. 2010 Turbulence modulation and drag reduction by spherical particles. *Physics of Fluids* **22** (8), 081702.

Paper 3

3

Orientation of nano-fibrillated cellulose in accelerated flow

By Karl Håkansson[1,2], Fredrik Lundell[1,2], Lisa Prahl Wittberg[1,2], Lars Wågberg[1,3] & L. Daniel Söderberg[1,2,4]

[1]Wallenberg Wood Science Center
[2] Linné Flow Centre, KTH Mechanics, SE-100 44 Stockholm, Sweden
[3] Fibre and Polymer Technology, Royal Institute of Technology, SE-100 44 Stockholm, Sweden
[4] Innventia AB, BOX 5604, SE-114 86 Stockholm, Sweden

May 15, 2012

The orientation of nano-fibrillated-cellulose, NFC, fibrils in an accelerated flow is studied both experimentally and numerically. NFC is a wood based material that due to its high stiffness, strength and abundance has high potential in future composites. A semi dilute water NFC dispersion is accelerated in a flow focusing channel system. The orientation is in the experiment determined via birefringence and compared through a quantitive order parameter S, to the 1-dimensional numerical study. The Smolushowski equation is solved numerically and the orientation distribution, during and after the acceleration is found. A material- and concentration dependent fitting parameter is found for one concentration, and the experiments and computations are shown to follow the same trends. The fibrils show a strong alignment in the direction of the flow during the acceleration, after which the orientation distribution homogenises again further downstream.

1. Introduction

Nano-Fibrillated Cellulose, NFC, is cellulose polymer bundles (fibrils) that exists as long chains in cellulose based materials *e.g.* wood. NFC was first extracted by Turbak *et al.* (1983) from wood. The biodegradable NFC has recently become more energy efficient to manufacture due to a pre-treatment of the wood pulp, described in Pääkkö *et al.* (2007). The NFC shows high potential for the use in composites with impressive properties, see *e.g.* Sehaqui *et al.* (2012); Iwamoto *et al.* (2011); Moon *et al.* (2011) and Walther *et al.* (2011).

The high potential and abundance of NFC makes it an interesting material to study. Here the focus is directed towards the behaviour of the rod-like fibrils in fluid flows, since fluid flows are present in different stages in most

material manufacturing processes, *e.g.* papermaking, extrusion or moulding. The properties of composites are highly correlated to the orientation of the fibers or fibrils in the material. And the fact that fluid flows have a large impact on the orientation distribution in the process makes it even more interesting to understand the mechanisms of the interaction between fluid and particles.

The orientation of suspensions containing rigid fibres or polymers in different flows has been considered analytically, experimentally and numerically *e.g.* Jeffery (1922); Trevelyan & Mason (1951); Batchelor (1970); Doi & Edwards (1986); Shaqfeh & Koch (1990); Petrie (1999); Krochak *et al.* (2008). There are not any universal models for describing dens particle suspension in fluid flows, and fitting parameters are still needed for most cases. This study is aimed on understanding the semi dilute regime and developing a simple experimental technique in order to qualitatively measure the orientation in a simple test geometry. Nevertheless, quantitative comparisons will be made.

Experiments in a flow focusing geometry, generating an extensional flow and at the same time minimising the shear, has been performed. The orientation of the NFC fibrils are studied before, during and after the acceleration with the help of birefringence. Numerical computations, containing one fitting parameter will be used and compared to the experiments. The fitting parameter in this case is a rotational diffusion coefficient, dependent on the shape, flexibility, chemical interactions and concentration of the particles.

This paper will first introduce the material NFC, thereafter the experimental setup will be discussed, followed by birefringence and alignment of rigid polymer-like rod theory. Finally the numerical computations, and an order parameter, connecting the experiments and computations will be described. Results from both experiments and computations will be shown and lastly the conclusions will be presented.

2. Method

2.1. *Nano-Fibrillated Cellulose, NFC*

Nano-Fibrillated Cellulose, NFC, are bundles of cellulose polymer chains (fibrils) extracted from wood, plants or bacteria. In this work, NFC from wood was used. The first step to extract the NFC is to disintegrate the wood cells and separate the fibrils from the lignin and the hemicelluloses. Turbak *et al.* (1983) demonstrated that this could be performed with a high pressure homogeniser.

Here, second generation (with surface charges) NFC, from Innventia AB was used. It was produced by Innventia AB, with the same process as described in Pääkkö *et al.* (2007), having widths, $d = 20 - 40$ nm, lengths, $l = 1 - 3$ μm and density $\rho = 1300$ kg/m^3. The dissolving pulp was looped through a slit homogeniser 10 times in order to obtain a water based gel with NFC concentration of 1% by weight. The sample was further treated by a ultra-sonic homogeniser to dilute and deflocculate the gel into a dispersion of concentration

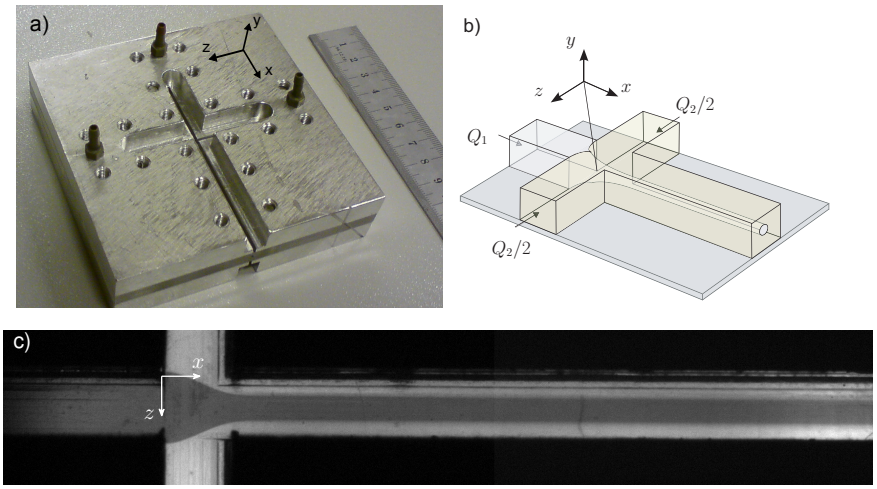

FIGURE 1. Photo (a) and schematic (b) of the flow apparatus. A visualisation image from the top of the channel is seen in (c), water is coming from the sides and focusing a water-ink mixture. The cross section of the channels are 1 mm^3.

0.15% by weight. Thereafter, the dispersion was put into a centrifuge with the aim to separate and remove large particles and obtain a clean sample. The NFC used is comparable to the NFC600 in Fall *et al.* (2011), with the difference of the concentration. The final concentration of the dispersion is 3 g/l corresponding to $nl^3 = 10 - 20$ (semi dilute) in all experiments, where n is the number of particles per volume. The NFC fibrils do not dissolve in water and are hence in a dispersion state. In the computations the fibrils are modelled as rigid rod like polymers.

2.2. *Flow apparatus*

Two syringe pumps transfer fluids into the focusing channel made out of Plexiglas, depicted in figure 1. The channel has a square cross section with height, $h = 1$ mm. There are three inlets, with length $45h$, and one outlet having the length $50h$. At the intersection of the three inlets in the channel, the two side flows focuses (accelerate) the core flow, figure 1b. The mass flow rate in the core channel is Q_1 and the total sheath flow is Q_2, see figure 1b. Here, $Q_1 = 6.5$ mm^3/s is constant and Q_1/Q_2 ranges from 0.23 to 6.8. A total of 25 cases has been captured. The flow is laminar with Reynolds numbers, Re$= Q_i h/\nu$ in the range of $5 - 50$, where ν is the viscosity of water.

A NFC dispersion is fed into the core channel, and depending on the purpose it is possible to use different liquids in the side channels. Here, distilled

water is used. The NFC dispersion is subjected to an acceleration when it is focused, which will be shown to orient the elongated particles (NFC) in the direction of the acceleration.

A camera, mounted on a microscope is used to capture images of the intersection part of the channel, in the x-z plane. An example image captured by the camera, is displayed in 1c, where water is focusing a water-ink mixture. The coordinate system is defined in figure 1b. The channel is placed between two crossed polarising filter in order to detect differences in birefringence of the NFC dispersion. The mean of 90 images was used for each experiment.

2.3. *Birefringence in a NFC dispersion*

Since the NFC fibrils are smaller than the wavelength of light, they can not be observed individually in the dispersion. However, with the use of polarised light, the birefringence of the sample can be detected. And from the birefringence the mean polymer or fibril orientation can be found and quantified. A polymer solution or dispersion can display a birefringent behaviour if the solution or dispersion is anisotropic, *i.e.* the orientation distribution of the polymers is not random. Experimentally, birefringence can be observed, and measured with the help of polarised light. To maximise the signal when the sample is placed between two crossed polarisation filters, the optical axis of the sample should be oriented at an angle of 45° with respect to the polarisation filters. In a polymer dispersion, the optical axis is in the direction where most polymers are aligned. Hence, the filters are oriented by a 45° offset to the x-direction.

The amount of light allowed to pass through the second filter is given by the following equation;

$$I(\Delta\theta) = I_0 \cos^2(\Delta\theta + \theta_0), \tag{1}$$

where I is the intensity, I_0 is the incoming light intensity, $\Delta\theta$ is the angle the sample has rotated the polarisation of the light and θ_0 is the angle between the polarisation filters, see Hecht (2002). Crossed polarisation filters means that $\theta_0 = 90°$ and the angle, $\Delta\theta$, can be calculated from;

$$\Delta\theta = \frac{2\pi d}{\lambda}|n_1 - n_2|, \tag{2}$$

where d is the thickness of the sample, λ is the wavelength of the incoming light, and n_1 and n_2 are the two different refractive indices.

By measuring the relative intensity, I/I_0, and the thickness, d, of the sample and knowing the wavelength, λ, it is possible to extract the difference of the refractive indices, Δn, from equation 1 and 2:

$$\Delta n = |n_1 - n_2| = \frac{\lambda}{2\pi d}\left(\cos^{-1}\sqrt{\frac{I}{I_0}} - \theta_0\right) \approx \frac{\lambda}{2\pi d}\sqrt{\frac{I}{I_0}}, \tag{3}$$

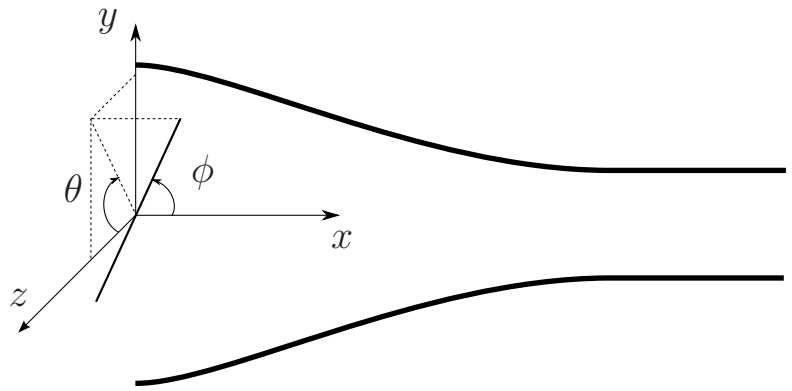

FIGURE 2. Schematic of the computation coordinate system and angles ϕ, θ defining the orientation of a fibril.

for small I, and $\Delta\theta << 90°$. In these experiments I_0 is unknown and Δn is compared with a reference birefringence, where Δn_{ref}, d_{ref} and I_{ref} are the refractive index difference, thickness and light intensity respectively, of a reference case. The relative birefringence is expressed as:

$$\frac{\Delta n}{\Delta n_{ref}} \approx \frac{d_{ref}}{d}\sqrt{\frac{I}{I_{ref}}}. \tag{4}$$

An increase of Δn is concluded to reflect an increase of the alignment, oriented 45° offset to the polarization filters.

2.4. *Particle rotation theory*

With the purpose of computing the orientation distribution evolution of the fibrils in space, affected by the biaxial accelerated flow in the channel and a rotational diffusion, the Smoluchowski equation is solved. The Smoluchowski equation is a diffusion equation with an extra force term, in the present study due to the fluid flow, see Doi & Edwards (1986). When the translational diffusion is neglected, the Smoluchowski equation takes the following form;

$$\frac{\partial \Psi}{\partial t} = \Re \hat{D_r} \cdot \Re \Psi - \Re \cdot \omega \Psi, \tag{5}$$

where $\Psi(\mathbf{r}, \mathbf{p}, t)$ is the orientation distribution, that is dependent on position, $\mathbf{r}$, orientation, $\mathbf{p}$, and time, t. The rotational diffusion coefficient is denoted $\hat{D}_r(\mathbf{p})$, ω is the angular velocity of the fibril and $\Re$ is the rotational operator:

$$\Re = \mathbf{r} \times \frac{\partial}{\partial \mathbf{r}}. \tag{6}$$

The orientation distribution along the centreline with symmetry for all θ is considered and the coordinate system is defined in figure 2. Assuming the fibrils to be inertial free, the flow to be steady and biaxial with a constant local acceleration and u to be the velocity in the x-direction, the the non-dimensional Smoluchowski equation becomes;

$$u^* \frac{\partial \Psi}{\partial x^*} = \frac{\partial}{\partial \phi} \hat{D}_r^* \frac{\partial \Psi}{\partial \phi} - \frac{\partial (\dot{\phi} \Psi)}{\partial \phi}, \tag{7}$$

where the superscript $(*)$ indicates a non-dimensionalised quantity, scaled with u and h.

The rotational diffusion constant is highly dependent on the concentration of fibrils, *i.e.* if the fibrils interacts with other fibrils during their rotation or if they rotate freely. In this study the system is in a semi-dilute state, which has been analytically studied for rigid polymers by Doi & Edwards (1986). The rotational constant in a dilute state, D_{r0}, was found to be:

$$D_{r0} = \frac{3 k_B T (2 ln(2 r_p) - 1)}{16 \pi \eta_s a^3}, \tag{8}$$

where k_B is Boltzmann's constant, T is the temperature, r_p is the aspect ratio, a is the half length of the fibril and η_s is the viscosity of the solvent. For a semi dilute case, the rotational constant increases due to particle-particle interactions and another formula in the same book was derived:

$$D_r = \beta D_{r0} (c 8 a^3)^{-2}, \tag{9}$$

here, c is the concentration and β is a constant that needs to be determined experimentally and it can be as large as 10^3, Doi & Edwards (1986). The final step is to account for the orientation of the fibrils, because if all fibrils are aligned, they will not interact with the neighbouring fibrils. This is also described in Doi & Edwards (1986) and the rotational diffusion constant, $\hat{D}_r$, is finally:

$$\begin{aligned} \hat{D}_r(\mathbf{p}) =& D_r \left[\frac{4}{\pi} \int \mathrm{d}\mathbf{p}' |\mathbf{p} \times \mathbf{p}'| \Psi_s(\mathbf{p}') \right]^{-2} = \\ =& D_r \left[8 \int \mathrm{d}\phi' \sin(\phi') |\sin(\phi')\cos(\phi) - \cos(\phi')\sin(\phi)| \Psi_s(\phi') \right]^{-2}, \end{aligned} \tag{10}$$

where Ψ_s is the orientation distribution of the surrounding fibrils.

The rate of change of the fibril orientation, $\dot{\phi}$, from the torque equations in the paper by Jeffery (1922), is in this flow given by:

$$\dot{\phi} = \frac{\partial \phi}{\partial t^*} = -\frac{\partial u^*}{\partial x^*} \left(\frac{r_p^2 - 1}{r_p^2 + 1} \right) \frac{3}{2} \cos(\phi) \sin(\phi). \tag{11}$$

Equation 7 was solved numerically with periodic boundary conditions using MATLAB.

2.5. *Order parameter*

In order to compare the fibril alignment in the experiments with the computations, the order parameter, S, defined in van Gurp (1995) as the mean of the second Legendre polynomial, P_2;

$$S = \langle P_2(\cos(\phi))\rangle = \left\langle \frac{3}{2}\cos^2(\phi) - \frac{1}{2} \right\rangle, \tag{12}$$

is used. This order parameter is a measure of the alignment of elongated particles in the x-direction, where $S = 1$ if all particles are aligned in the x-direction and $S = 0$ if the distribution is random. When the distribution is known, as it is in the computation, S is calculated as:

$$S_{comp} = \int_0^{\pi} \Psi(\phi) \left(\frac{3}{2}\cos^2(\phi) - \frac{1}{2} \right) \sin(\phi) \mathrm{d}\phi \int_0^{2\pi} \mathrm{d}\theta, \tag{13}$$

and is normalised according to:

$$\int_0^{\pi} \Psi(\phi) \sin(\phi) \mathrm{d}\phi \int_0^{2\pi} \mathrm{d}\theta = 1. \tag{14}$$

In van Gurp (1995), it is shown that the order parameter, S, can be deduced from the birefringence of a sample, using the formula:

$$S_{exp} = \frac{\Delta n}{\Delta n_{max}}. \tag{15}$$

The parameter S is normalised with a reference, S_{ref}, since I_0 and Δn_{max} are unknown. The reference case is chosen to be $Q_2/Q_1 = 1.15$, which is the experiment closest to $Q_2/Q_1 = 1$.

3. Results and Discussion

3.1. *Fibril orientation from the experiments*

The first experiment was conducted with water in all channels in order to capture a background image, see figure 3a. The background image is subtracted from all experimental images. The original and final image for case $Q_2/Q_1 = 1.15$ is shown in figures 3b and 3c, respectively.

Final images are shown in figure 4, where a 3 g/l NFC dispersion is used in the core channel and water is flowing in the side channels. The focusing region is viewed in the x-z-plane through crossed polarisation filters. The flow rate of the NFC dispersion, $Q_1 = 6.5$ mm^3/s, is kept constant while the water flow rate, Q_2, is increased from (a) to (e). The light intensity increases (here assumed to be linear) as the orientation of NFC in the flow direction increases. In the region upstream of the focusing, the light intensities are close to constant for all five cases. The fact that there are a preferred alignment upstream of the acceleration is due to the shear, which is strongest close to the walls. On the other hand, downstream of the acceleration, as the flow rate of Q_2 is increased,

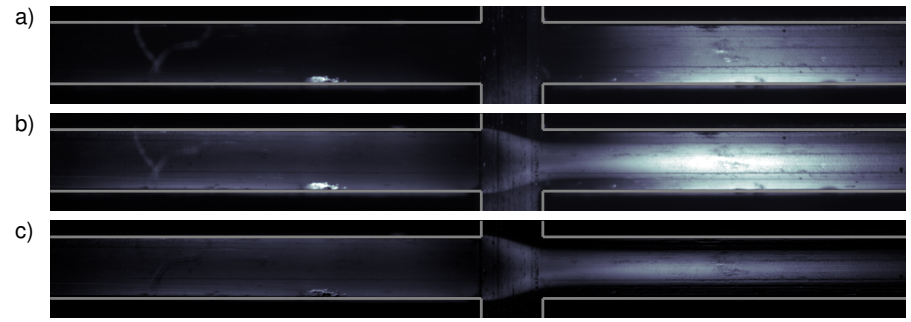

FIGURE 3. Background image (top), where only water is used, and original measurement image, $Q_2/Q_1 = 1.15$ (middle). The final image, where the background image is subtracted from the measurement image (bottom).

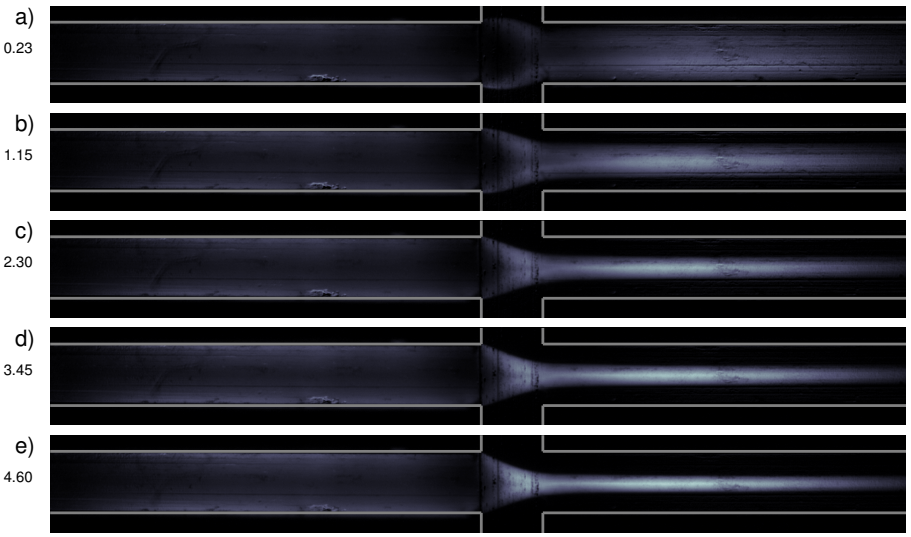

FIGURE 4. Images from the experiment at different degree of acceleration elongation, where the numbers on the left of each image correspond to the value of Q_2/Q_1 for that case.

the orientation (light intensity) of the NFC is increased. More acceleration is found to correspond to a higher degree of orientation.

It is found in figure 4 that the intensity in the upstream region is slightly changing comparing the experiments. A feature believed to be due to the light source or the Plexiglas, since Q_1 is kept constant. The intensities of the full

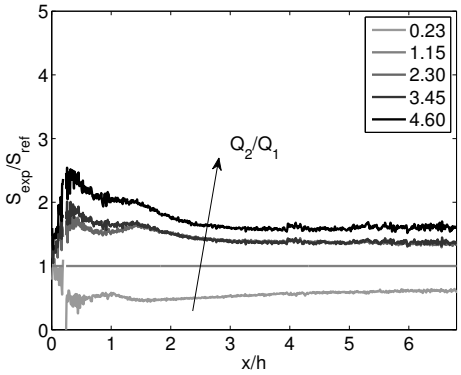

FIGURE 5. The order parameter S_{exp}/S_{ref} for the experiment.

image are therefore normalised by the sum of the intensities extracted from the upstream region.

The relative order parameter is calculated using equations 4 and 15;

$$\frac{S_{exp}}{S_{ref}} = \frac{\Delta n}{\Delta n_{ref}} \approx \frac{d_{ref}}{d}\sqrt{\frac{I}{I_{ref}}}. \tag{16}$$

The thickness d was determined from the images. Figure 5 shows the relative order parameter for five of the total 25 cases. The relative order parameter is demonstrated to increase as the acceleration is increased.

3.2. *Estimating the streamwise velocity distribution from the images*

The velocity and acceleration at each downstream position are found for each experimental case from the corresponding experimental images, in figure 6a the case $Q_2/Q_1 = 1.15$ is seen. The sharp intensity edge is found for each column in the image with a simple thresholding method. The continuous line shown in figure 6b is a best-fit fourth order polynomial. The core flow is assumed to have a square cross section, and from the decrease in cross section, the velocity, $u(x)$, figure 6c, and acceleration, $a(x)$, figure 6d, are estimated. The velocity is estimated as;

$$u(x) = \frac{Q_1}{h^2}\left(\frac{d(x_0)}{d(x)}\right)^2. \tag{17}$$

3.3. *Fibril orientation from the computations*

Equation 7 is solved numerically using the experimental velocity distributions $u(x)$. The parameters are set to $c = 0.3\%$, $r_p = 100$, $a = 1$ μm, $\eta_s = 10^{-3}$, $h = 1$ mm, $T = 293$ K, $\beta = 200$. In figure 7, the orientation distribution, Ψ,

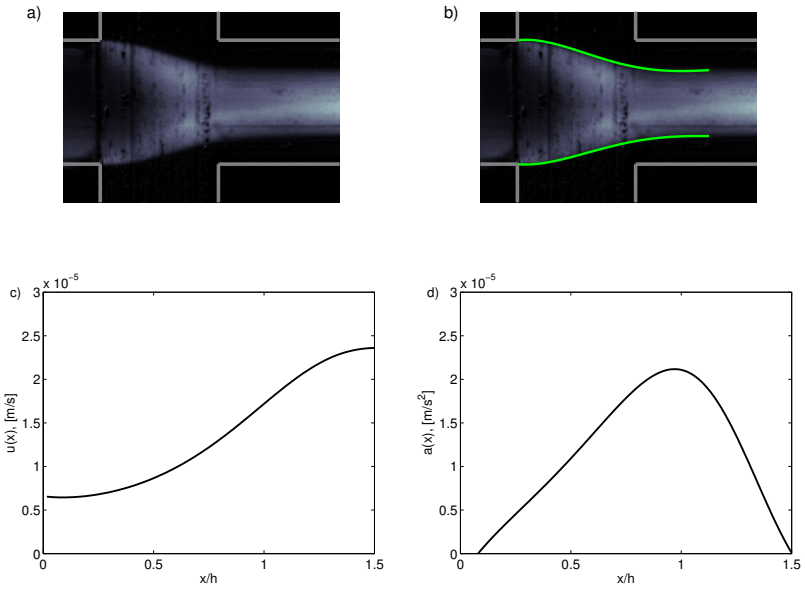

FIGURE 6. (a) A close up of the experimental case $Q_2/Q_1 = 1.15$ and the detected edge marked in (b). The velocity increase (c) and the acceleration (d), calculated from the edge found in (b), where the cross section is assumed to be square.

versus downstream position at the centreline of the channel is seen in 7a and the order parameter, S_{comp}, from equation 13 versus downstream position is seen in 7b, for the $Q_2/Q_1 = 1.15$ case.

The fibrils are in figure 7 seen to align in the x-direction during the acceleration, but as soon as the acceleration is stopped at $x/h \approx 1.2$, *cf.* 7b, the diffusion will drive the distribution to become more homogeneous.

4. Discussion

Figure 8 depicts the order parameter, S_{comp}, from equation 13 for the different downstream positions and accelerations. The figure shows a large alignment increase during the acceleration, followed by a slow relaxation. The alignment is enhanced for a stronger acceleration. The experimental relative order parameter results is shown in 9a and the numerical in 9b. There are two distinct differences between figures 9a and 9b, (i) the peak close to the start of the acceleration is not as distinct in the experiment and (ii), the experiment shows a larger difference of the order parameter for increasing acceleration. Note that the behaviour after the acceleration is similar. Figure 10 displays the order parameter for the experiment (dashed line) and the computation (full line) at

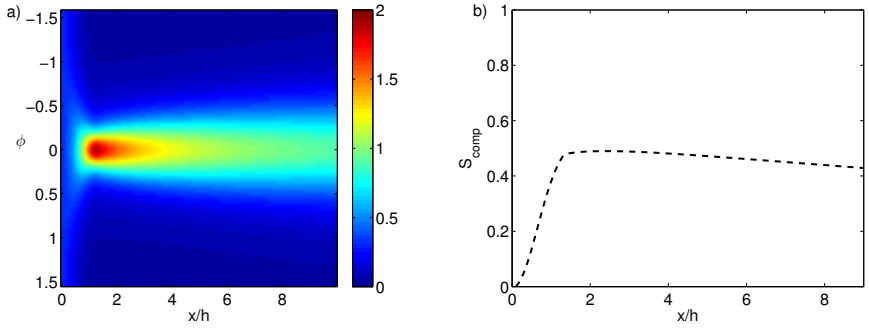

FIGURE 7. The orientation distribution function Ψ is shown for different downstream positions with $Q_2/Q_1 = 1.15$ in (a). In (b), the order parameter S_{comp}, calculated from Ψ in (a), is displayed for downstream positions.

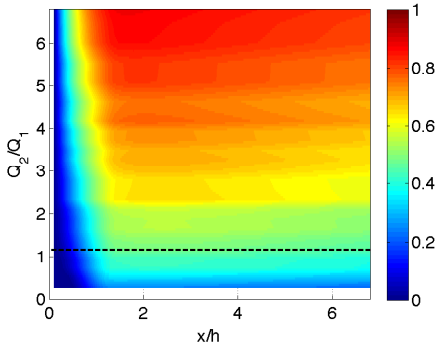

FIGURE 8. The order parameter from the computations, S_{comp} defined in equation 13.

the downstream position $x/h = 6.8$, for increasing accelerations. The experiments only deviates from the computation for high accelerations. What should not be forgotten is that the computation is only for the centreline, while the experiment is the projection seen from the top of the channel, and that the alignment is assumed to be lowest on the true centreline. It can be expected that the alignment is less pronounced on the centreline compared to further out from the centre. This arises from the fact that close to the walls the shear gives rise to a pre-orientation of the fibrils upstream of the acceleration. Thus, the average alignment in the centre slice will be larger than on the actual centreline. The agreement between the experiments and the computations is only

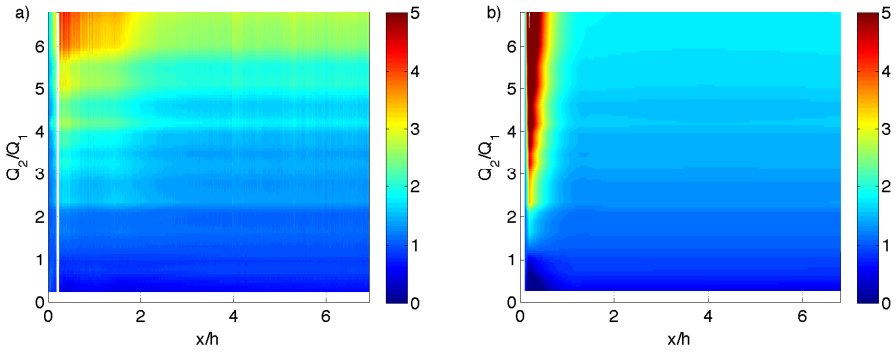

FIGURE 9. Relative order parameter, S/S_{ref}, for (a) experiments and (b) computations.

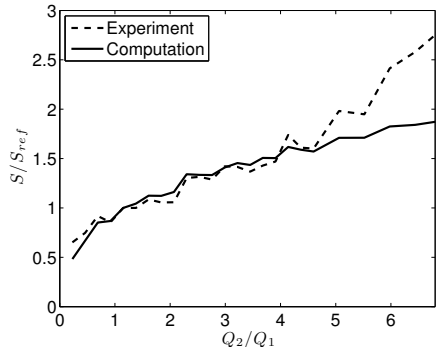

FIGURE 10. The order parameter at the downstream position $x/h = 6.8$ from the experiments, dashed line, and the computations, full line, for different accelerations.

qualitative. Anything else, however, would be remarkable due to the simplifications regarding (i) velocity distribution and (ii) particle interactions in the present model.

The parameter β is adjusted to fit the experimental data. In the study by Teraoka *et al.* (1985), it was shown that β increases from unity to a value of between 10^3 and 10^4 with increasing concentration. Changing β changes the relaxation time. The value $\beta = 200$ was found to fit the present measurements best and are in line with previous suggestions.

5. Conclusions

The orientation distribution of Nano-Fibrillated Cellulose fibrils in an accelerated flow are studied experimentally, by measuring the relative birefringence of the NFC dispersion at different accelerations. The fibrils align in the extensional flow and remain aligned far downstream. The Smolushowski equation for the orientation distribution in one dimension is solved numerically and compared with the experiments. The NFC fibrils are observed to align in the flow direction during the acceleration and to slowly become more random downstream of the acceleration, for both cases. The two methods shows similar trends, but the computation shows a lower degree of alignment at high accelerations. In the rotation diffusion term, a fitting parameter β is needed, here found to be of the order 10^2, in accordance to other studies for a semi dilute suspension.

The most important features, that the fibrils orient in the x-direction due to the acceleration and that the fibrils do not immediately relax back to a random state is shown to correspond well with theory. The details of the process is out of the scope of the present model.

Acknowledgements

A. Fall is greatly acknowledged for the assistance and preparation of the clean NFC dispersions, and the fruitful discussions. Inneventia AB is greatly acknowledged for providing the nano-fibrillated cellulose. M. Kvick is greatly acknowledged the rewarding discussions. This work was funded by the Knut and Alice Wallenberg Foundation, through the Wallenberg Wood Science Center. Dr. Lundell and Dr. Prahl Wittberg has also been funded by the Swedish Research Council.

References

Batchelor, G. K. 1970 Slender-body theory for particles of arbitrary cross-section in stokes flow. *J of Fluid Mech* **44** (03), 419–440.

Doi, M. & Edwards, S. 1986 *The theory of polymer dynamics*. Oxford University Press Inc.

Fall, A. B., Lindström, S. B., Sundman, O., Ödberg, L. & Wågberg, L. 2011 Colloidal stability of aqueous nanofibrillated cellulose dispersions. *Langmuir* **27**, pp. 11332–11338.

van Gurp, M. 1995 The use of rotation matrices in the mathematical description of molecular orientations in polymers. *Colloid Polym Sci* **273**, pp. 607–625.

Hecht, E. 2002 *Optics*, 4th edn. Addison Wesley.

Iwamoto, S., Isogai, A. & Iwata, T. 2011 Structure and mechanical properties of wet-spun fibers made from natural cellulose nanofibers. *Biomacromolecules* **12**, pp. 831–836.

Jeffery, G. B. 1922 The motion of ellipsoidal particles immersed in a viscous fluid. *Proceedings of the Royal Society of London. Series A, Containing Papers of a Mathematical and Physical Character* **102** (715), pp. 161–179.

Krochak, P. J., Olson, J. A. & Martinez, D. M. 2008 The orientation of semidilute rigid fiber suspensions in a linearly contracting channel. *Phys Fluids* **20** (7), 073303.

Moon, R. J., Martini, A., Nairn, J., Simonsen, J. & Youngblood, J. 2011 Cellulose nanomaterials review: structure, properties and nanocomposites. *Chem. Soc. Rev.* **40** (7), 3941.

Pääkkö, M., Ankerfors, M., Kosonen, H., Nykänen, A., Ahola, S., Österberg, M., Ruokolainen, J., Laine, J., Larsson, P. T., Ikkala, O. & Lindström, T. 2007 Enzymatic hydrolysis combined with mechanical shearing and high-pressure homogenization for nanoscale cellulose fibrils and strong gels. *Biomacromolecules* **8**, pp. 1934–1941.

Petrie, C. 1999 The rheology of fibre suspensions. *J of Non-Newtonian Fluid Mech.* **97**, 369–402.

Sehaqui, H., Mushi, N. E., Morimune, S., Salajkova, M., Nishino, T. & Berglund, L. A. 2012 Cellulose nanofiber orientation in nanopaper and nanocomposites by cold drawing. *Appl. Mater. Interfaces* **4**, pp. 1043–1049.

Shaqfeh, E. S. G. & Koch, D. L. 1990 Orientational dispersion of fibers in extensional flows. *Phys Fluids* **2**, pp. 1077–1093.

Teraoka, I., Ookubo, N. & Hayakawa, R. 1985 Molecular theory on the entanglement effect of rodlike polymers. *Phys Rev Lett* **55**, pp. 2712–2715.

Trevelyan, B. J. & Mason, S. G. 1951 Particle motions in sheared suspensions. i. rotations. *J of Colloid Sci* pp. 354–367.

Turbak, A., Snyder, F. & Sandberg, K. 1983 Microfibrillated cellulose, a new cellulose product: properties, uses, and commercial potential. *J Appl Polym Sci: Appl Polym Symp* **37**, pp. 815–827.

Walther, A., Timonen, J. V. I., Diez, I., Laukkanen, A. & Ikkala, O. 2011 Multifunctional high-performance biofibers based on wet-extrusion of renewable native cellulose nanofibrils. *Advanced Materials* **23**, pp. 2924–2928.